



LUND
UNIVERSITY

Master of
Science Thesis
VT2016

Validation of the Eclipse(TM) Treatment Planning System for Synchrotron Microbeam Radiotherapy

Madeleine Holm

Supervision

Crister Ceberg, Jeffrey Crosbie and Per Engström

This work has been performed at
School of Science, RMIT University, Melbourne, Australia

Department of Medical Radiation Physics,
Clinical Sciences, Lund
Lund University

Cancer är den andra vanligast dödsorsaken i världen idag, näst efter hjärt-kärlsjukdom. Varje år insjuknar nästan 13 miljoner människor av cancer och även om dödigheten minskar i takt med att forskningen går framåt så finns det ännu cancersjukdomar som inte går att bota. I Sverige ges strålbehandling till hälften av alla som drabbas av cancer och står för 30 % av all cancerbot.

Vid en strålbehandling bestrålar man det område på kroppen där cancercellerna sitter med joniserande strålning. Joniserande strålning verkar genom att förstöra cellers DNA så att de dör. När man bestrålar en tumör med joniserande strålning så kommer man inte bara att träffa tumörcellerna utan också omkringliggande frisk vävnad. Men eftersom frisk vävnad i regel är mer motståndskraftig mot joniserande strålning än tumörvävnad så kan man se till att ge en stråldos som är tillräckligt stor för att ta död på tumören och samtidigt tillräckligt liten för att omkringliggande frisk vävnad ska överleva. Detta fungerar dock inte för alla tumörer. Olika former av tumör och normalvävnad är olika mycket känsliga för strålning och vissa tumörer går inte att bestråla då de sitter nära frisk vävnad som är mycket strålkänslig eller då tumören själv är okänslig för strålning.

MRT står för *Microbeam Radiation Therapy* och är en ny form av strålbehandling som använder sig av strålning producerad i en synkrotron (en partikelaccelerator som kan producera högintensiv joniserande strålning) i form av mycket tunna strålnippen separerade från varandra, så kallade mikrostrålar. Det tycks vara så att cancerceller är mycket känsliga för den här sortens strålning samtidigt som friska celler är mycket motståndskraftiga mot den. Att använda den här sortens strålning till cancerbehandlingar skulle alltså kunna möjliggöra behandling av tumörtyper som man tidigare inte kunnat bota.

Hittills har man enbart bestrålat försöksdjur med mikrostrålar, men målet är att börja med kliniska försök på människor inom en inte allt för avlägsen framtid. Innan man kan göra detta finns dock ett antal problem att lösa. Ett av dessa är att man behöver ett så kallat dosplaneringsprogram, ett datorprogram som utifrån en röntgenbild av en patient beräknar hur stor stråldos olika delar av kroppen får då den bestrålas. Man förlitar sig på dessa beräkningar då man ska bestämma hur mycket strålning som ska ges till en patient, och det är därför mycket viktigt att beräkningarna blir rätt för att man inte ska ge för låg eller för hög dos, då en för låg dos kan resultera i att tumören inte försvinner och en för hög dos i att patienten får sjukdomar som följd av att den friska vävnaden fått mer strålning än vad den klarar av.

De dosplaneringsprogram som för närvarande finns fungerar inte för MRT, utan ett nytt program måste utvecklas. Detta har nyligen gjorts vid RMIT i Melbourne Australien. I det här arbetet används programmet för att beräkna dos i olika föremål, så kallade fantom, bestående av vatten samt av material tillverkat för att efterlikna mänsklig vävnad. Denna dos jämförs med mätdata från samma föremål för att se om stråldoserna som programmet beräknar är korrekta.

1 Abstract	4
2 Background.....	5
2.1 Microbeam Radiation Therapy.....	5
2.2 The proposed clinical workflow of Microbeam Radiation Therapy	7
2.2.1 Prescribing of Microbeam Radiation Therapy	7
2.2.2 A Treatment Planning System for Microbeam Radiation Therapy	8
2.2.3 Monte Carlo simulations of microbeams in MRT	10
3 Materials and Methods.....	11
3.1 The Eclipse Treatment Planning System	11
3.1.1 Dose calculation algorithm	11
3.2 Treatment Planning Calculations.....	14
3.2.1 Homogenous water phantom	14
3.2.2 Inhomogeneous tissue equivalent phantoms.....	14
3.2.3 Obliqueness.....	15
3.3 Monte Carlo Simulations	15
3.4 Ion Chamber Measurements.....	15
3.5 Radiochromic film measurement and readout	17
4 Results	18
4.1 Homogeneous water phantom	18
4.1.1 Percentage depth-dose curves	18
4.1.2 Field profiles	30
4.2 Inhomogeneous phantoms	32
4.3 Obliquity	38
5 Discussion and Conclusion	38
6 References	41

1 Abstract

This work presents the first data from a calculation engine for synchrotron Microbeam Radiation Therapy (MRT) implemented in the Eclipse™ Treatment Planning System from Varian Medical Services. The calculation engine constitutes a simple pencil beam algorithm estimating ‘peak’ dose and of Monte Carlo simulated Peak Valley Dose Ratios (PVDRs) that are used to obtain ‘valley’ dose. The aim of this work is to benchmark data calculated using Eclipse against measured and Monte Carlo simulated data in order to enable future clinical applications of the calculation engine.

Percentage Depth Dose (PDD) curves and field profiles in a homogeneous water phantom as well as PDD curves and point dose values in inhomogeneous, tissue equivalent phantoms were calculated. These data were compared against data measured using a PTW 31014 Pin-Point ionization chamber and GafChromic HD-V2 film as well as against Monte Carlo data simulated using the GEANT4 toolkit.

The data show that Eclipse performs very well in calculating ‘peak’ dose in a homogeneous water phantom and that it calculates ‘valley’ dose with some accuracy, although an underestimation of valley dose for smaller field sizes and an overestimation for larger field sizes is discovered. This is found to depend on the inability of Eclipse to account for the field size dependence of the peak to valley dose ratio (PVDR). Field profiles are also calculated with reasonable accuracy, although due to the simplistic nature of the algorithm used to calculate dose it does not completely calculate dose deposition from a synchrotron radiation X-ray beam. This simplification results in errors in the field profiles. When it comes to simulating dose in inhomogeneous mediums, Eclipse is struggling. The Eclipse calculated ‘peak’ dose distributions in phantoms containing lung equivalent tissue do not agree with Monte Carlo simulations or with what you would theoretically expect. Furthermore, for the ‘valley’ dose, an error in the algorithm causes the deposited dose to inexplicably drop to zero in some regions of the phantom for some phantom configurations.

Although there are limitations in the calculation engine in Eclipse and although there is still work to be done, the data generated in this work are overall encouraging and indicate that with further improvements there are possibilities and potential for this calculation engine to be implemented in the clinic in the future.

2 Background

2.1 Microbeam Radiation Therapy

The idea of using microbeams to perform radiation therapy is based on an experiment performed in the 1960s, when, in preparation for a potential manned space flight, Curtis investigated the biological effect of heavy cosmic ray particles by irradiating mouse brain tissue with very thin ($25 \mu\text{m}$), very intense (on the order of hundreds of Gy) deuteron beams. Surprisingly they found that normal tissue tolerates high doses of this irradiation extremely well. In most cases the rays seemed to have no effect at all on brain tissue. In fact, the dose had to be raised to 4000 Gy in order to see any tissue-effects (degeneration of neurons in the beam path) on the mouse brain tissue at all (Curtis, 1967).

In 1992 Slatkin *et al.* proposed a new method to carry out radiotherapy based on these results. They suggested the cross-firing synchrotron-produced lattices of $25 \mu\text{m}$ wide dose-peaks separated by $50 - 200 \mu\text{m}$ into a target. They called their method Microbeam Radiation Therapy (MRT). Their idea was that this technique would raise the therapeutic index (the ratio of the amount of radiation that has sufficient tumor effect and the amount that causes normal tissue toxicity) since the radiation doses could be kept below the threshold for radiation damage outside the interlacing region (the target) while having damaging effects inside the target (Slatkin *et al.*, 1992).

The technique of MRT uses a lattice of synchrotron-generated highly collimated, quasi-parallel x-ray microbeams approximately $25 - 50 \mu\text{m}$ wide and separated with $200 - 400 \mu\text{m}$ center-to-center distances (c-t-c). The small divergence in the microbeams together with the rather low energies used (normally $100 - 200 \text{ keV}$) entails an extremely high dose gradient between the peak- and valley-regions in the lattice. The so-called peak dose (the dose directly in the peak regions) is usually as high as several hundreds of Gy, while the valley dose (the dose in the valley regions between the peaks) is significantly smaller. The ratio between peak and valley dose is referred to as the Peak-Valley Dose Ratio (PVDR) and is in the order of $20 - 100$. Figure 1 shows a typical field-profile for a microbeam field used for MRT.

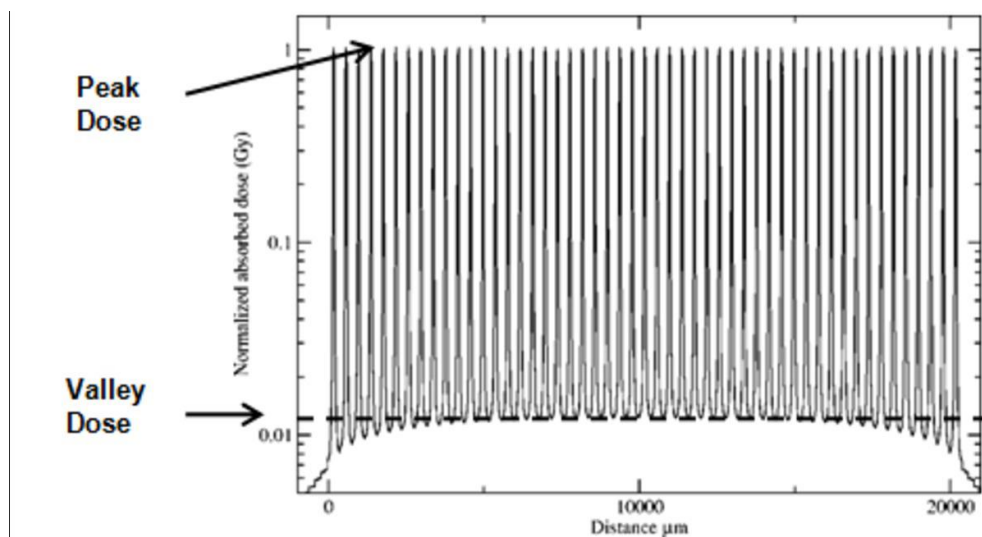


Figure 1 – Representation of an array of microbeams for MRT obtained by Monte Carlo simulation. Image obtained from Fournier *et al.* Copyright of this image lies within the authors (Fournier *et al.*, 2014).

In order to avoid blurring of the dose-profiles due to organ motion the dose rate has to be extremely high (typically 250 Gy s^{-1} at 5 mm depth in water for a $20 \times 20 \text{ mm}^2$ field in clinical mode at the Imaging and Medical Beamline (IMBL) at the Australian Synchrotron in Melbourne, Australia and about 7000 Gy/s for the same configuration at the European Synchrotron Radiation Facility (ESRF) in Grenoble, France). The beam produced by the synchrotron X-ray source is a fan beam with vertical width of about 1 mm and a horizontal width of about 30 mm. Thus, the target has to be scanned vertically through the beam during irradiation in order to create square fields.

In 2002 Dilmanian *et al.* irradiated rats with implanted gliosarcoma tumors using microbeam lattices with different peak-doses and c-t-c distances. They found that the normal tissue effects and survival rate of the rats appeared to be independent of peak-dose and c-t-c distance but correlate with valley dose. The brain-sparing effects that microbeam radiation has compared to broad-beam radiation vanished only when the valley dose approached tissue tolerance level for broad beam radiation (Dilmanian *et al.*, 2002). The exact radiobiology behind this is not yet completely known although some theories suggest that the Bystander effects as well as the higher migration of tumor cells in comparison to normal tissue are possible contributing factors (Dilmanian *et al.*, 2003, Dilmanian *et al.*, 2002, Crosbie *et al.*, 2010, Dilmanian *et al.*, 2007). The microvascular hypothesis is another strong theory for understanding the unique radiobiology of MRT, particularly for brain and CNS irradiations. The microvascular hypothesis suggests malignant blood vessels are less competent than healthy tissue at repairing the damages that the high dose microbeams cause at repairing the high dose damage from the X-ray microbeams compared to healthy musculature (Bouchet *et al.*, 2013, Bouchet *et al.*, 2015).

A number of successful animal trials have been conducted in MRT, entailing that the next step in MRT research should be the initiation of clinical trials on veterinary and human patients (Regnard *et al.*, 2008, Bouchet *et al.*, 2010, Laissue *et al.*, 2013). Before this step can be reached however there are a number of obstacles to overcome, one of which being the implementation of an MRT-specific Treatment Planning Systems (TPS). The distinct features of beam generation, beam characteristics and irradiation geometry of MRT render the existing TPSs for radiation therapy unsuited for MRT. The work described in this thesis focuses on the verification of a commercial treatment planning system (Eclipse™ by Varian Medical Systems) in which a synchrotron beamline machine has been added and a simple pencil beam kernel algorithm has been implemented.

2.2 The proposed clinical workflow of Microbeam Radiation Therapy

The typical clinical workflow of conventional radiation therapy treatment, from diagnosis to delivery of treatment, is illustrated in Figure 2.

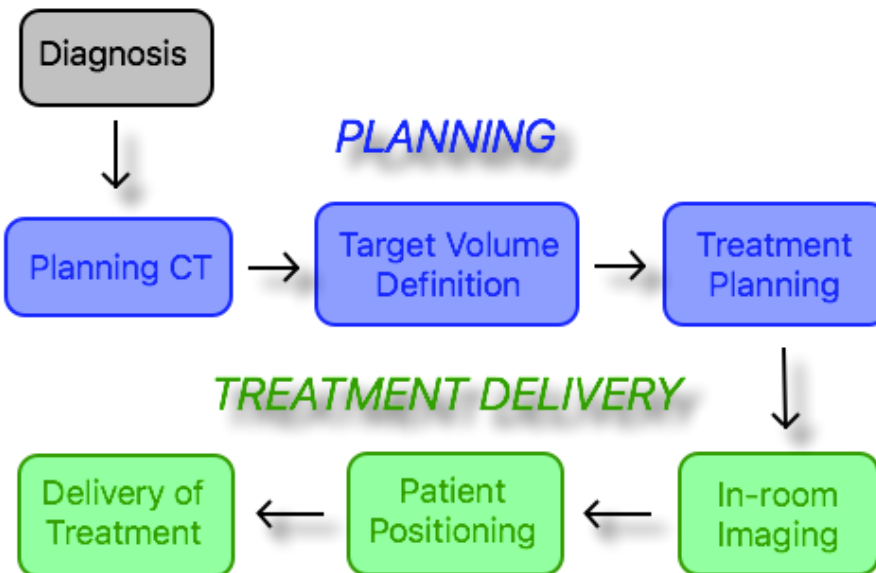


Figure 2 - The clinical workflow of a radiation therapy treatment

In order to successfully implement MRT in the clinic, all of the points in Figure 2 have to be considered. The long-term aim of the synchrotron radiotherapy research project in Australia is to translate conventional clinical protocols to the synchrotron beamline in order to enable **a clinical implementation of MRT**. These protocols include the following: basic dosimetry, treatment planning, image-guidance, patient positioning, irradiation, and record and verify methods. The focus of this study is on the treatment planning aspect.

2.2.1 Prescribing Microbeam Radiation Therapy

In conventional broad beam radiation therapy, the target and the organs at risk (OAR) are defined in the preparatory CT images acquired of the patient. The treatment is subsequently prescribed by defining upper and lower dose limits to the target and to the OARs. However, due to the distinctive field characteristics in MRT the treatment prescription method has to be modified. It is not yet settled whether the prescription should be based on peak-dose, valley dose, PVDR or a combination of these.

One suggestion is to prescribe dose based on valley dose. This suggestion is based on the fact that while peak dose will always be high enough to kill all cells exposed to it, which may render the magnitude of it rather unimportant, the magnitude of the valley dose seems to be fundamental for the long-term toxicity in normal tissue (Dilmanian et al., 2002). In 2010 Martinez-Rovira *et al.* used the theory of Dilmanian *et al.*, together with known tolerance levels for normal tissue to define safe irradiation protocols for MRT. They performed Monte-Carlo simulations to evaluate the maximum peak and valley doses achievable in tumors while keeping the valley dose in healthy tissue below the tolerance level. They found that for a centrally located tumor (at a depth of 7.2 cm) the maximum peak and valley dose achievable was 55 Gy and 2.6 Gy respectively if the maximum valley dose to skin, bone and healthy brain tissue was to be within the tolerance levels (5 % probability of complication within 5 years). (Martinez-Rovira et al., 2010).

In 2012 Anderson *et al.* performed an evaluation of a number of dose-volume metrics for MRT. They pointed out that when valley dose is used as a metric, a local minimum has normally been considered. Since the local minimum is a point-dose metric that does not take volume into account, valley dose alone can be considered a limited metric for MRT since the biological effects of MRT seem to be volume dependent. They therefore suggested three other metrics for MRT: the PMVDR (peak to mean-valley dose ratio), the mean dose or a percentage of the volume below certain threshold doses, which are all volumetric measures. However, it remains to be investigated if any of these measures will offer an improved clinical outcome compared to the valley dose metric (Anderson et al., 2012).

2.2.2 A Treatment Planning System for Microbeam Radiation Therapy

Modern Treatment Planning Systems (TPS) for external beam therapy takes beam configuration, irradiation geometry and attenuation information from Computed Tomography (CT) images as input and uses incorporated algorithms to output dose distribution over the patient volume. The distinct features of beam generation and irradiation geometry of MRT render the existing algorithms in TPSs for radiation therapy unsuitable for MRT and therefore an MRT specific TPS is required.

In 2012, Martínez-Rovira *et al.* developed a calculation engine that was to be used in an MRT specific TPS. The engine was based on the Monte Carlo code PENELOPE. In radiation transport, Monte Carlo methods treat each particle track as a sequence of stochastic processes, where random numbers and probabilities determine path-length, scattering angles etc. The PENELOPE code enables simulation of photon and electrons transport in a wide energy range and arbitrary material systems. The generation and transport of particles through the beamline and the interactions inside a head-sized water phantom were simulated and compared to measurements using radiochromic films. Three different field sizes were used ($1 \times 1 \text{ cm}^2$, $2 \times 2 \text{ cm}^2$ and $3 \times 3 \text{ cm}^2$) and the microbeam size was $50 \mu\text{m}/400 \mu\text{m}$ ($50 \mu\text{m}$ wide microbeam peaks separated with a $400 \mu\text{m}$ c-t-c distance). Simulations agreed with measurements both regarding percentage depth dose and PVDR within the calculated uncertainties (Martinez-Rovira et al., 2012).

Once validation was complete dose-calculations in a virtual model of a dogs head obtained from a CT-scan was performed. A virtual tumor was placed at a depth of 4-5 cm and the relative uncertainties in peak and valley dose at this position were found to be in the order of 1.2 % and 1.9 % respectively. When a bin size of approximately $10 \mu\text{m}$ in the transversal direction of the beam was used, the simulation took slightly less than a day to execute (Martinez-Rovira et al., 2012).

In his PhD thesis, Bartzsch described his efforts to develop an MRT specific TPS. He used two Monte Carlo methods to simulate dose distribution from an MRT-source in a voxelized target (such as a CT-image). Initially he used a forward method that simply simulates each particle track as a sequence of stochastic processes. The problem using this method is that the voxelized structure must be very small ($< 5 \mu\text{m}$) in order to simulate the rapid spatial variations in the dose in MRT. This entails a large amount of statistical noise, and requires a large amount of histories to be simulated in order to obtain statistically significant results, resulting in very long simulation times (Bartzsch, 2014).

Therefore he also suggested a so-called semi-adjoint method, which tracks particles backwards from the area where they are detected to the source of radiation. This approach requires less calculation power than a forward simulation since many of the simulated photons in a forward simulation doesn't actually hit the detecting volume considered and are therefore simulated unnecessarily. It can however only be used in certain fixed geometries and it is still rather time

consuming and therefore this method is not optimal for creating a calculation engine in a TPS (Bartzsch, 2014).

Consequently Bartzsch also suggested an analytical method based on point-dose kernels. Dose calculations were performed using a kernel-based convolution algorithm. While the disadvantage of this method is that the precision is lower, the advantage is that it is a lot less time-consuming than Monte Carlo based methods. Bartzsch tested the method of using point-dose kernels by simulating an irradiation of a homogeneous water phantom with a field of 50 μm /400 μm microbeams and compared the results to Monte Carlo simulations. The analytical method was found to agree well with Monte Carlo simulations for peak doses but worse for valley doses, especially for shallow depths and in inhomogeneous areas, although the precision could be improved by deforming the geometry of the phantom in which simulation was performed. Bartzsch implemented the analytical dose-kernels in the VIRTUOUS platform (University of Heidelberg, Germany) to create a TPS with a graphical user interface (GUI) (Bartzsch, 2014).

In 2014 Poole *et al.* implemented a kernel-based algorithm in the commercially available Eclipse™ TPS from Varian Medical Systems (v11.0.31). His aim was to create a TPS that would be easy to fit into the clinical workflow and since Eclipse is one of the most widely used TPS in clinics today being able to use its interface for MRT treatment planning would achieve this. The work of Poole *et al.* is not yet published; it only exists as a manuscript in preparation (Poole et al., 2015).

In this work, an MRT-specific Monitor Unit (MU) is defined. The MU is a measure of machine output. The MU is the unit in which information about the described dose is sent from the TPS to the treatment machine. For conventional linear accelerators the MU is calibrated in terms of dose delivered to a reference point under reference conditions, typically so that 100 MU gives 1 Gy at 10 cm depth in water for a 10 x 10 cm² field size, and during treatment delivery the number of MU delivered is measured using an ion chamber in the gantry. For MRT however, Poole *et al.* suggested a MU expressed in units of time instead of dose. The dose delivered for MRT depends on the beam height, scan speed and instant dose rate, but since the dose rate at the Australian synchrotron is kept constant for all MRT purposes, it does not have to be encapsulated in the MU. Information about the dose rate does not have to be sent from the TPS to the synchrotron. Since the dose is directly proportional to beam-height and inversely proportional to scan-speed, the unit of the MU will be seconds and the MU will be a direct measure of the time a point of the target will spend within the beam.

A simple pencil beam algorithm was implemented to display an estimate of the intensity of dose deposited within the CT dataset. The algorithm was not used for exact characterization of peak and valley dose since the scale of the CT set is much larger than the scale of the microbeams thus such a characterization would only result in aliasing. Moreover this method would result in non-optimal computational performance. Instead, peak dose, valley dose and PVDR are displayed separately in the TPS. In the algorithm, calculated peak dose is approximated to be proportional to primary dose (dose deposited by primary particles). The peak dose actually constitutes of primary dose and scattered dose from the valley regions, but since the scattered dose is small in comparison to the primary dose this approximation can be considered valid. Since primary dose is proportional to broad beam dose, the algorithm calculates the broad beam dose deposited within the CT data set, which can give an estimate of the intensity of peak dose within this data set. Valley dose is then simply obtained dividing the peak dose with Monte Carlo simulated PVDRs.

Poole *et al.* implemented the kernel-based algorithm in Eclipse and used it to generate treatment plans. However, the utility of the TPS remain to be tested. Therefore the aim of this work is to benchmark the relative dose predictions from the Eclipse TPS to actual measurements previously conducted at the IMBL at The Australian Synchrotron as well as to Monte Carlo simulations. It is important to note that the work done by Poole *et al.* is still a work in progress. The version of the algorithm used today is under development and is changed continuously while it is being tested (Day, 2015).

2.2.3 Monte Carlo simulations of microbeams in MRT

Monte Carlo simulations have always played an important role when it comes to investigating dose distributions in MRT. In fact, the work by Slatkin *et al.* from 1992 that first suggested using microbeams as a therapy method mainly consisted of Monte Carlo simulations and ever since Monte Carlo simulations have played an important role when it comes to researching MRT (Slatkin *et al.*, 1992).

In radiation transport, Monte Carlo methods treat each particle track as a sequence of stochastic processes, where random numbers and probabilities determine path-length, scattering angles etc. In early applications the Monte Carlo code used for the simulations of microbeams was usually the ESG4-code. Nowadays however, either the GEANT4 or the PENELOPE codes are normally used since they have proven to provide more accurate results for low energies. Both of these codes simulates transport of electrons and positrons at low energies, which is necessary in order to accurately simulate the high dose gradients in MRT (Spiga *et al.*, 2007, Cornelius *et al.*, 2014).

Slatkin *et al.* did the first work on Monte Carlo simulations and MRT during the invention of MRT. They simulated microbeams with c-t-c distances of 50, 100 and 200 μm in a water tank in order to investigate the obtained dose distributions. Since this publication, various other simulations have been performed on water tanks investing how variating different irradiation parameters impacts the dose distribution (Slatkin *et al.*, 1992, Nettelbeck *et al.*, 2009, Bartzsch *et al.*, 2014, Siegbahn *et al.*, 2006). Monte Carlo simulations have also been used to simulate dose-distributions from MRT in tissue-phantoms. In 1998 Company and Allen calculated dose distribution in a tissue/lung/tissue phantom and different research groups have carried out various simulations on human and animal head phantoms (Company and Allen, 1998, Martinez-Rovira *et al.*, 2010, Orion *et al.*, 2000).

Monte Carlo simulations have previously been suggested as a plan verification tool for e.g. Volume Modulated Arc Therapy (VMAT). The difficulties when implementing Monte Carlo simulation as a verification tool for MRT involves the lower energies used and the need for dose calculation on a micrometer scale. In 2014 Cornelius *et al.* developed a Monte Carlo code for simulating dose distribution and suggested it would be used for treatment plan verification. The code models the ID17 biomedical beamline at the European Synchrotron Radiation Facility in Grenoble, France. Their code was benchmarked against a previous model of the same beamline and against measurements on a water tank, and good agreement was found. The authors argued that since Monte Carlo simulations are the most accurate method of dose determination in MRT it is the best-suited method for plan verification (Cornelius *et al.*, 2014, Boylan *et al.*, 2013).

In his master's thesis work from 2015, Day used the GEANT4 toolkit to simulate broad beam and microbeam irradiations of a water phantom at the IMBL at the Australian synchrotron in order to investigate parameters of dosimetric interest for MRT. He defined a single slit collimator collimating the beam height, a multislit collimator and a field-defining mask to mimic the setup at the IMBL at the Australian Synchrotron and he simulated irradiations on the

water phantom of a $10 \times 1 \text{ mm}^2$ and a $20 \times 1 \text{ mm}^2$ field of synchrotron radiation. Through convolution methods data for irradiations of a $10 \times 10 \text{ mm}^2$ and a $20 \times 20 \text{ mm}^2$ field were also obtained. Percentage Depth-Doses (PDDs) and field profiles were extracted from the simulated data for analyzing purposes. The data produced by Day is used in this work to compare against simulated data from the TPS of Poole *et al.* (Day, 2015)

3 Materials and Methods

3.1 The Eclipse Treatment Planning System

The Eclipse treatment planning system from Varian Medical Systems is one of the most widely used treatment planning systems in the world today. It has an intuitive, user friendly Graphic User Interface (GUI) with easy ‘drag and drop’ tools which enables it to be used by a large number of staff members at the clinics working with it. Due to this ease of use, Eclipse is familiar to many nurses, radiotherapists, oncologists and medical physicists working with radiation therapy today. It would thus greatly simplify the clinical implementation of MRT if the GUI of Eclipse could be used to create treatment plans for MRT.

3.1.1 Dose calculation algorithm

An advantage of The Eclipse treatment planning system is that it allows the user to access all the data and functions that the system uses for dose calculation. This is something that many other TPSs don’t allow you to do. Moreover the Eclipse software package includes an Algorithm Application Programming Interface (API) through which users can implement their own dose calculation algorithms. In 2015 Poole *et al.* implemented an algorithm in the API for calculating dose-depositions from microbeam fields at the IMBL at the Australian synchrotron. This work is not yet published; it only exists as a manuscript in preparation (Poole et al., 2015).

The algorithm does not quantify absorbed dose absolutely, it only gives an estimate of the relative dose deposited within the CT data set. Absolute doses are subsequently obtained by normalizing the calculations to a point or volume of the data set.

During dose calculations, the peak dose is assumed to be proportional to the total energy released per unit mass (TERMA) since the contributions from scattered radiation in the peak regions is small compared to that of primary particles. Because broad beam dose is also proportional to TERMA, the peak dose will be proportional to the broad beam dose (via the MRT collimator output factor). Thus, by calculating broad beam dose over the CT data set one can obtain an estimate of the intensity of peak dose deposited over the CT data set. In the calculation engine, pencil beam kernels are used to calculate broad beam dose as described by Storchi and Woudstra (Storchi and Woudstra, 1996, Storchi *et al.*, 1999, Storchi and Woudstra, 1995).

A full description of the derivation of the pencils beam kernels is beyond the scope of this work since myself, the candidate, was not involved in the development or implementation of them. This text will instead be limited to a brief general explanation of the concept of dose calculation using pencil beam kernels.

2D convolution of pencil beam kernels is a quicker, less computationally demanding alternative to 3D convolution of point-dose kernels (Storchi and Woudstra, 1995). A pencil kernel describes the energy deposition in a medium around a line monodirectional beam and can be derived from either measured beam data or Monte Carlo simulations (Ceberg *et al.*, 1996). When calculating dose using pencil beam kernels one convolves the fluence pattern of the incident radiation field with a pencil beam kernel (Ahnesjo and Aspradakis, 1999). The

algorithm by Storchi and Woudstra on which this work is based uses two kernels: the ‘scatter kernel’ and the ‘boundary kernel’. The scatter kernel is used to calculate depth dose and the boundary kernel describes dose at the field boundaries and is used to produce off-axis ratio profiles (Storchi and Woudstra, 1995).

To account for inhomogeneities in the medium, the calculation of peak dose uses radiological depth, d_{rad} , to calculate the water-equivalent depth at which the current voxel can be considered to reside. The radiological depth is given by equation (1), where d_i is the physical depth of the voxel in material i with density ρ_i and ρ_{water} is the density of water.

$$d_{rad} = \frac{\sum_{i=1}^n d_i \cdot \rho_i}{\rho_{water}} \quad (1)$$

Since the relative dose will change during acceleration and deceleration of the target **when scanning it vertically through the beam**, a weighting factor can be applied to the calculated dose to account for changes away from the nominal scan-speed of the target.

To obtain valley dose, the peak dose for every voxel is simply divided with the PVDR for that voxel according to equation (2). To find the PVDR for a specific voxel, the radiological depth is used together with and a Monte Carlo simulated curve of PVDR as a function of depth.

$$D_{valley} = \frac{D_{peak}}{PVDR} \quad (2)$$

It's important to keep in mind the simplistic nature of this dose calculation method. Due to numerous approximations made, it is expected that it will not perform optimally for all situations and the accuracy of the TPS will be limited by this fact.

Since the resolution of the CT data set is significantly poorer than the microbeam structure, displaying the actual microbeams over the CT data set would only result in aliasing. Due to this limitation, the peak dose, valley dose and PVDR are never displayed at the same time over the CT-data set. Instead the user can choose to calculate peak-dose, valley dose or PVDR for a defined field configuration. Figure 3 shows the Eclipse interface with calculated doses for a field of synchrotron radiation incident on a water phantom.

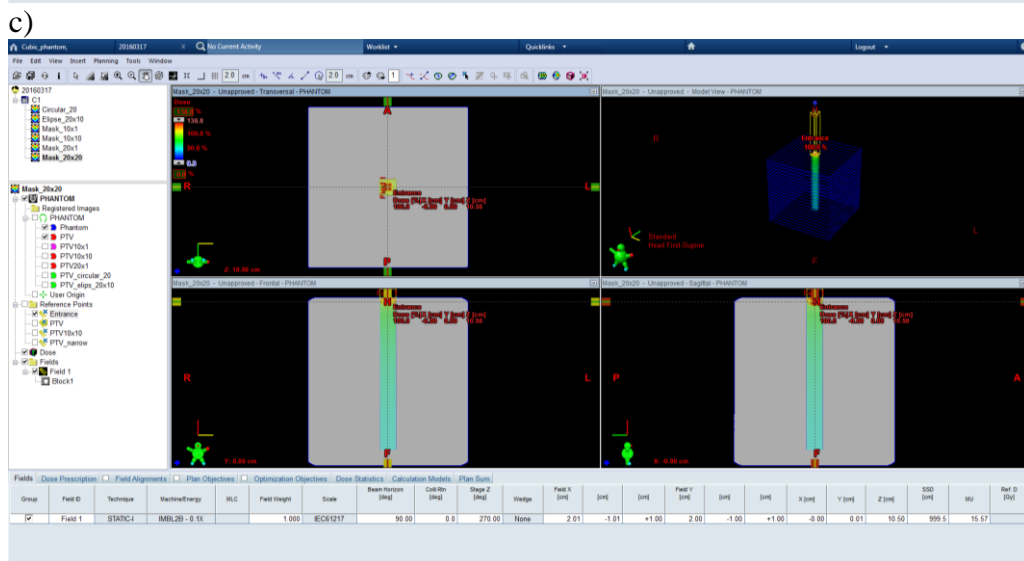
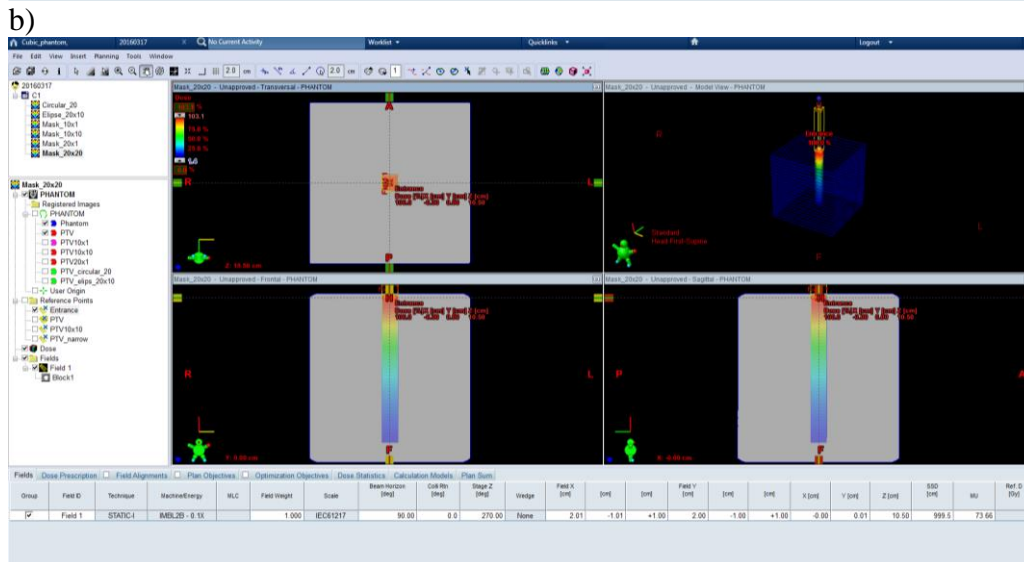
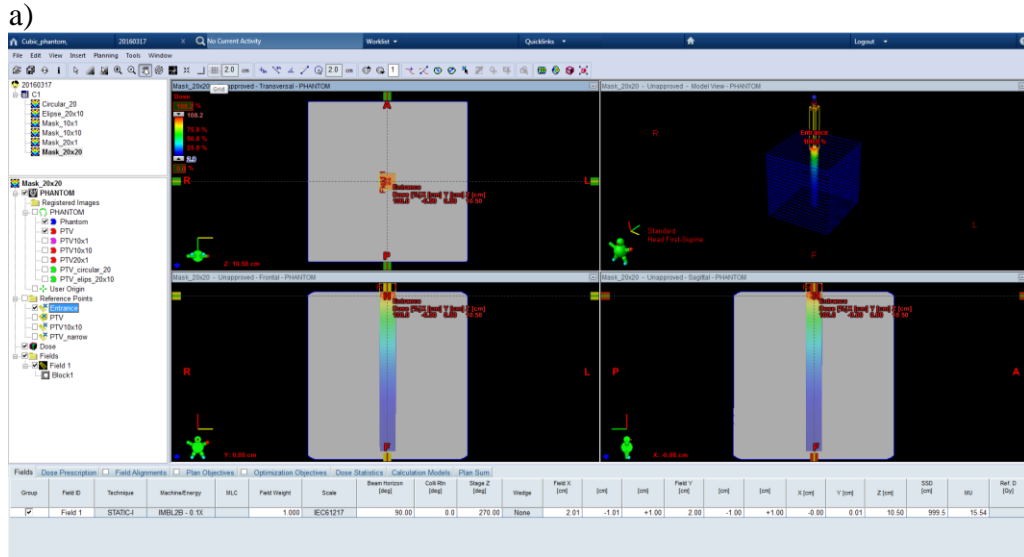


Figure 3 – The interface of the Eclipse based TPS for MRT. The figure shows deposited a) peak dose, b) valley dose and c) PVDR from a 20×20 mm 2 field of synchrotron radiation incident on a $200 \times 200 \times 200$ mm 3 water phantom.

3.2 Treatment Planning Calculations

3.2.1 Homogenous water phantom

In order to investigate the performance of Eclipse in homogeneous material, a $200 \times 200 \times 200$ mm 3 cubic water phantom (HU = 0) was defined in the contouring workspace of Eclipse. Irradiations of the water phantom were calculated for rectangular field of field sizes of 10×1 mm 2 and 20×1 mm 2 as well as for square fields of field sizes of 10×10 mm 2 and 20×20 mm 2 . All field were incident orthogonal to the phantom surface. From the calculated dose grid Percentage Depth Dose (PDD) curves were exported. Moreover for the 10×10 mm 2 and the 20×20 mm 2 fields horizontal and vertical dose profiles at 0 mm, 10 mm and 20 mm depth in the phantom were exported.

3.2.2 Inhomogeneous tissue equivalent phantoms

Several inhomogeneous phantoms were created in Eclipse in order to investigate how well Eclipse would perform in calculating the dose to inhomogeneous material. The phantoms were created to mimic existing Solid Water and tissue equivalent slabs from GAMMEX Inc. (California, USA). The following slabs were mimicked: the 457-202 Solid Water (SW) slab, the 450-202 SB3 Cortical Bone (CB) slab, the 456-205 IB3 Inner Bone (IB) slab and the 455-210 LN-300 Lung Equivalent (LE) slab.

In order to define volumes mimicking these materials in Eclipse, their CT-values in Hounsfield Units (HU) had to be known. Eclipse uses calibration curves relating physical density, electron density and a number of other physical quantities to HU since these quantities are needed in order to perform dose calculation over the different areas of the CT image. For a clinically used system these calibration curves are obtained through imaging objects with known physical properties with the CT scanner used for treatment planning imaging. For this system, however, being purely research based, the calibration curves are standardized curves representing a standard CT scanner. When defining a phantom material in Eclipse, one needs to feed Eclipse the CT value corresponding to the physical density, electron density and other physical quantities of the material (Schneider et al., 1996).

To find the correct HU for the GAMMEX slabs that were to be mimicked, the electron density to HU and physical density to HU calibration curve were extracted from Eclipse and by using the electron density and physical density for the slabs (provided by the manufacturer) the correct HU of the slabs could be found. Since two slightly different HU for each slab were found (one from the electron density to HU calibration curve and one from the physical density to HU calibration curve) the used HU were averages over these two.

Five different phantoms were defined according to Table 1. The phantoms were all irradiated with a 10×10 mm 2 field of synchrotron radiation incident orthogonal to the phantom surface and PDDs were exported from the calculated dose grid. From the calculated peak dose grids, point doses where also exported at the same depth in the phantoms as where the point dose measurements with the ion chamber was taken (see section 4.2) and the dose ratio between dose in the inhomogeneous phantom and dose at the same depth in water were calculated.

Table 1 – The inhomogeneous phantoms used for measurements and calculations. The phantoms were created using Solid Water and tissue equivalent slabs from GAMMEX. The following slabs used: the 457-202 Solid Water (SW) slab, the 450-202 SB3 Cortical Bone (CB) slab, the 456-205 IB3 Inner Bone (IB) slab and the 455-210 LN-300 Lung Equivalent (LE) slab.

Phantom name	Phantom construction
Solid Water phantom	20 mm SW
Lung phantom	10 mm LE + 10 mm SW
Bone phantom	5 mm IB + 10 mm SW
Simplex Chest Wall (SCW) phantom	12 mm SW + 20 mm LE + 12 mm SW
Complex Chest Wall (SCW) phantom	2 mm SW + 2.5 mm CB + 5 mm IB + 2.5 mm CB + 20 mm LE + 12 mm SW

3.2.3 Obliqueness

To investigate how well Eclipse could handle fields incident on the phantom surface in a non-orthogonal manner, fields incident with different angles from the normal were also calculated. A $100 \times 100 \times 50$ mm³ homogeneous water phantom was irradiated with a 10×10 mm² field of synchrotron incident at angles 0° , 5° , 10° and 20° from the normal. From the calculated peak dose grids, point doses were also exported at 35 mm depth in the phantoms in order to obtain the dose ratio between dose deposited by the oblique fields and dose at the same depth deposited by an orthogonal field.

3.3 Monte Carlo Simulations

Monte Carlo simulations of irradiations of the solid water phantom described in section 3.2.1 had previously been performed by Day in his master's thesis work (Day, 2015). He used the GEANT4 toolkit to define a similar setup as the one used at the IMBL at the Australian Synchrotron and then simulated irradiations of a homogeneous water phantom. He used an energy spectrum that ranged from 38.60 keV to 389.3 keV and with a mean energy of 101.9 keV. This is similar to the photon energies used in the TPS. The cut-off ranges in water were set to 10 μ m for photons, electron and **positrons**, corresponding to cut-off energies of 990 eV and 14.0874 keV for photons and **for electrons and positrons** respectively. Peak dose and valley dose were simulated for a 10×1 mm² and a 20×1 mm² field. Data was also obtained for a 10×10 mm² and a 20×20 mm² field through convolution methods.

To obtain some data that could be compared to the Eclipse-calculations of dose in inhomogeneous phantoms, Day also used his Monte Carlo setup to simulate irradiations of the SCW phantom described in section 3.2.2. In this simulation a 10×10 mm² field of monoenergetic 100 keV microbeams was used together with the same cut off energies as mentioned earlier to irradiate the phantom.

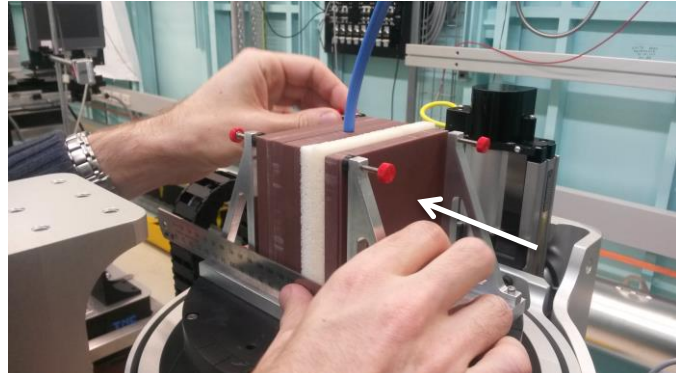
3.4 Ion Chamber Measurements

The extracted PDD curves from the calculated data were compared to measured PDD curves. The measurements were carried out in 2015 by other RMIT university researchers (not myself the candidate). Measurements were performed using a PTW 31014 Pin-Point ionization chamber. This is a cylindrical, waterproof ionization chamber produced for measurements on small radiation fields. It has a radius of 1 mm and a length of 5 mm. The sensitive volume of the chamber is 0.015 cm³ (PTW, 2012).

A PTW MP1 liquid water phantom was used for the PDD measurements. The ion chamber was placed in the tank and the central axis of the chamber was carefully aligned with respect to the incident horizontal beam. The water tank has an accessory that allows the user to manually and accurately position the ion chamber at different depths in the tank with respect to the incident radiation beam. The tank was positioned onto a motorized stage (Huber, Germany), which scanned the tank vertically through the beam for each measurement.

In addition to the liquid water tank measurements, **the tissue equivalent phantoms in Table 1 where used** for point dose measurements in inhomogeneous materials. The ion chamber was inserted into a cavity specially drilled into the solid water slabs and the phantoms were scanned vertically through the beam for each measurement. The phantom consisting of Solid Water slabs was also rotated with respect to the beam exit port in order to obtain measurements for oblique field angles. The experimental setup for the SCW and CCW phantoms are shown in Figure 4. The point dose for the inhomogeneous phantoms and oblique field measurements were divided with point dose at the same depth for an orthogonal field incident at a homogeneous water phantom in order to obtain dose ratios that could be compared to calculated dose ratios.

a)



b)

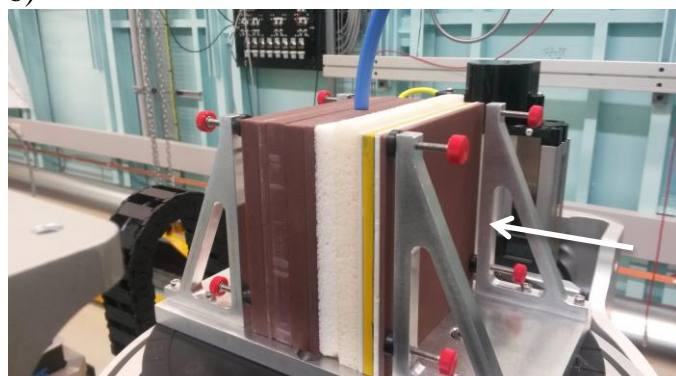


Figure 4 – The experimental setup for the SCW and CCW phantoms. The ion chamber is inserted in a cavity specially drilled into the solid water slabs. The white arrows in the images indicate the incoming beam direction.

The uncertainty in the ionization chamber measurement was estimated to be 2 % of the measured value. This is a conservative estimate of the precision with which the experiment was expected to be able to be replicated from a true independent measurement.

Due to the size of the sensitive volume of the chamber, it cannot be used to measure peak and valley dose in a microbeam field. Instead, the measurements were performed on a broad beam field. Since in a microbeam field, the fraction of dose from scattered radiation in the peaks is very small, broad beam dose can be considered comparable to peak dose. Thus the measured

broad beam doses were compared to calculated peak doses. An output factor directly links the broad beam dose with the peak dose for absolute dosimetry purposes (Day, 2015)

3.5 Radiochromic film measurement and readout

Characterization of the field profiles was performed by irradiation of radiochromic film (Devic et al., 2016). The films were irradiated at the IMBL at the Australian synchrotron in 2015 by RMIT university researchers whilst the subsequent film scanning was performed by myself, the candidate. Three films were irradiated with a $10 \times 10 \text{ mm}^2$ field of 40 Gy broad beam synchrotron radiation and three films were irradiated a $20 \times 20 \text{ mm}^2$ field of 112 Gy of broad beam synchrotron radiation. For the purpose of irradiation, the films were placed in a solid water phantom at depths of 0 mm, 10 mm and 20 mm.

Radiochromic film consists of monomer crystals (active component) in a gel bound to a mylar substrate. When the film is irradiated the monomer undergoes partial polymerization, which causes the film to change color. By scanning the film, the amount of light transmitted through it can be measured. This amount is proportional to the absorbed dose. Radiochromic film can thus be used to estimate absorbed dose, although in these measurements it was only used to obtain relative dose profiles (Crosbie et al., 2008).

The film used was the GafChromic HD-V2 film from Ashland (New Jersey, USA). This film is suitable for measurements of synchrotron irradiation due to its large dynamic dose range (from 10 to 1000 Gy). Many other film types would saturate at doses much lower than this. The HD-V2 film has a high spatial resolution ($5 \mu\text{m}$) although in this experiment the spatial resolution was limited by the scanner resolution rather than the film resolution. The energy dependence of the film is minimal between 100 keV up to MV range (Ashland).

The active component in GafChromic films is a chain of fatty acids similar to stearin and belonging to the diacetylene class of molecules. Combined with a marker dye, stabilizers and other components these acids constitute the active layer of the film, which is coated on a clear polyester substrate as shown in Figure 5. Since the film is asymmetrical, Ashland warns that the response of the measurements made with a scanner may be dependent on which side of the film is facing the light source and they therefore advise the user to be consistent with the positioning of the film during scanning (Crosbie et al., 2008, Ashland).

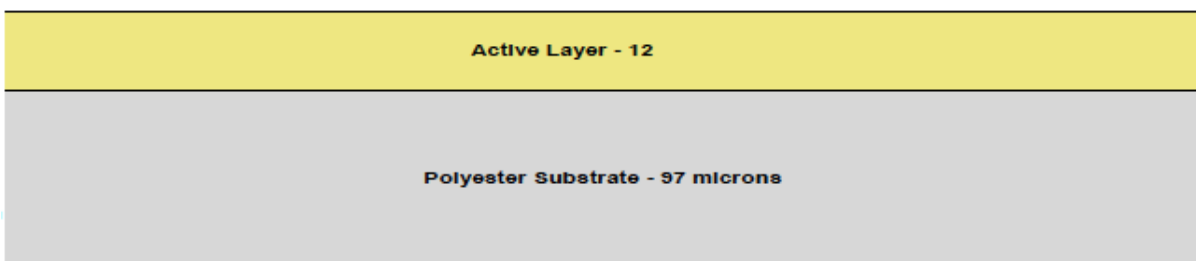


Figure 5 - Configuration of GafChromic HD-V2 dosimetry film(Ashland).

Post irradiation, the films were scanned using an EPSON Desktop scanner with a resolution of 600 ppi = $42 \mu\text{m}$. The films were placed in a film holder before scanning and the active layer of the film was consistently facing the light source in order to exclude any response dependence due to the asymmetry of the film. The image data obtained from scanning was corrected for uneven illumination using a “rolling ball” algorithm in ImageJ. This algorithm determines a local background value for every pixel by averaging over a large number of pixels and then it subtracts this value from the original image. Subsequently the remaining background was subtracted; the mean value of a region of interest well outside the field was found and subtracted

from the image. From the film data, horizontal and vertical field profiles were exported and then compared to calculated data.

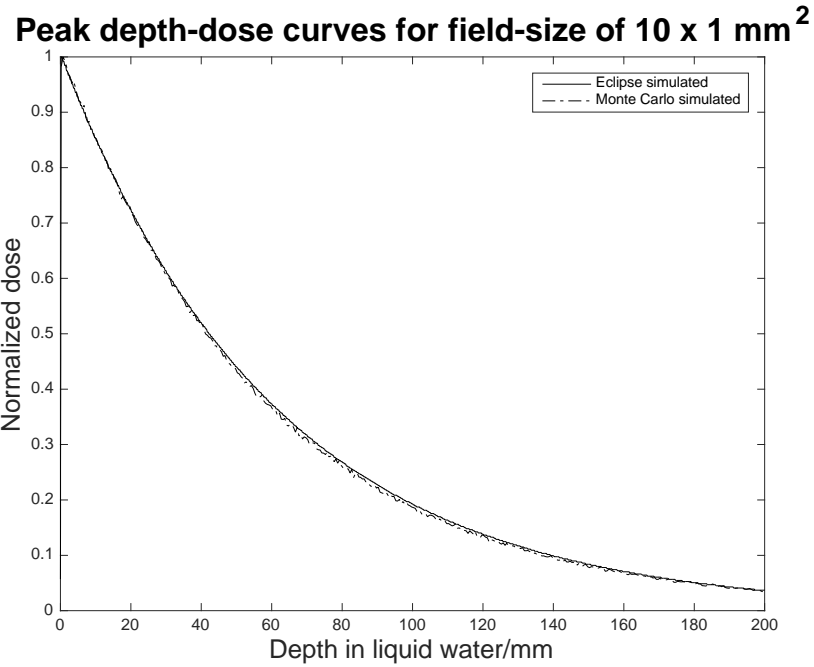
4 Results

4.1 Homogeneous water phantom

4.1.1 Percentage depth-dose curves

Eclipse calculated and Monte Carlo simulated peak PDDs for a $10 \times 1 \text{ mm}^2$, a $20 \times 1 \text{ mm}^2$, a $10 \times 10 \text{ mm}^2$ and a $20 \times 20 \text{ mm}^2$ field of synchrotron radiation orthogonally incident on a cubic $200 \times 200 \times 200 \text{ mm}^3$ water phantom are shown in Figure 6 to Figure 9. For the $10 \times 10 \text{ mm}^2$ and $20 \times 20 \text{ mm}^2$ fields the measured PDDs are also displayed. The figures show that for the $10 \times 1 \text{ mm}^2$ and the $20 \times 1 \text{ mm}^2$ fields there is an excellent agreement between Eclipse-calculated and Monte Carlo simulated data where the only deviation between the curves seem to be due to statistical noise in the Monte Carlo simulations. For the $10 \times 10 \text{ mm}^2$ field the agreement between Eclipse calculated and Monte Carlo simulated data is also good. The agreement between Eclipse-calculated and measured data is rather good as well. The calculated data tends to slightly underestimate dose although it lies mostly within the error bars of the measured data. For the $20 \times 20 \text{ mm}^2$ field the calculated data somewhat underestimates dose compared to Monte Carlo simulated and measured data.

a)



b)

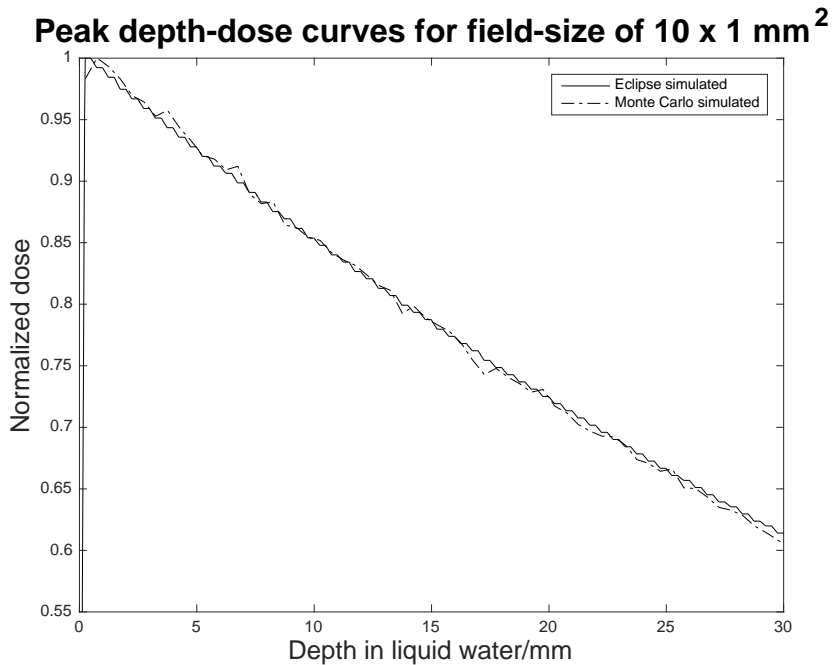
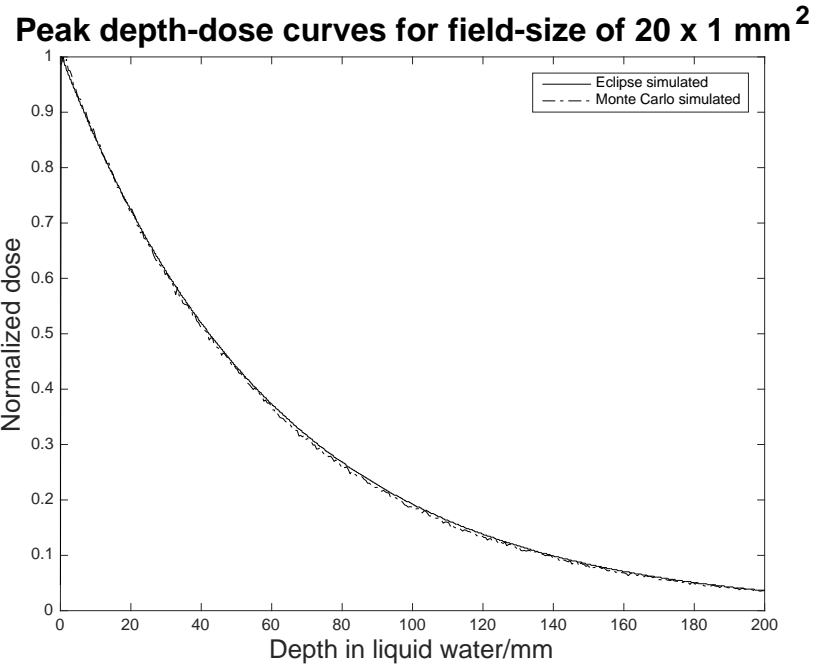


Figure 6 - Percentage Depth-Dose Curves for a $10 \times 1 \text{ mm}^2$ field of synchrotron peak-dose radiation incident on a $200 \times 200 \times 200 \text{ mm}^3$ liquid water phantom. The figure shows Eclipse-calculated and Monte Carlo simulated data. All data are normalized to the maximum value of the data set. The curves display both the entire water-phantom a), and an enlargement of the first 30 mm b). The figure shows an excellent agreement between Eclipse-calculated and Monte Carlo simulated data where the only deviations between the curves seem to be due to statistical noise in the Monte Carlo simulations.

a)



b)

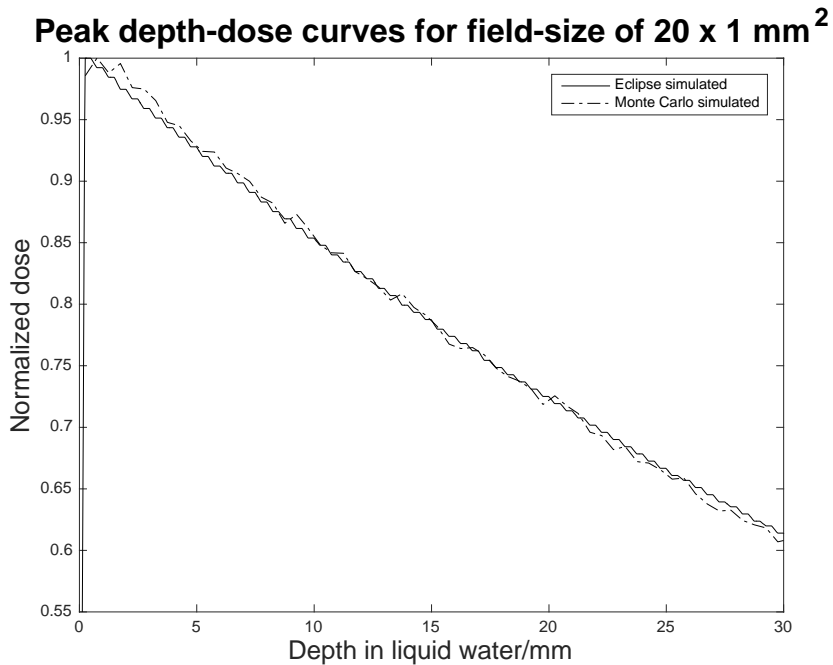
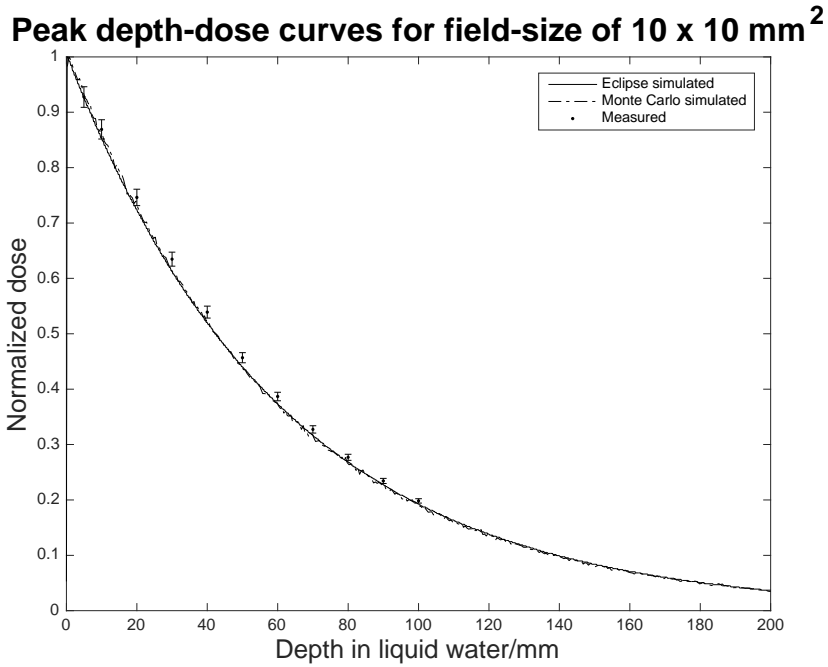


Figure 7 - Percentage Depth-Dose Curves for a $20 \times 1 \text{ mm}^2$ field of synchrotron peak-dose radiation incident on a $200 \times 200 \times 200 \text{ mm}^3$ liquid water phantom. The figure shows Eclipse-calculated and Monte Carlo simulated data. All data are normalized to the maximum value of the data set. The figure shows both the entire water-phantom a), and an enlargement of the first 30 mm b). The curves display an excellent agreement between Eclipse-calculated and Monte Carlo simulated data where the only deviation between the curves seems to be due to statistical noise in the Monte Carlo simulations.

a)



b)

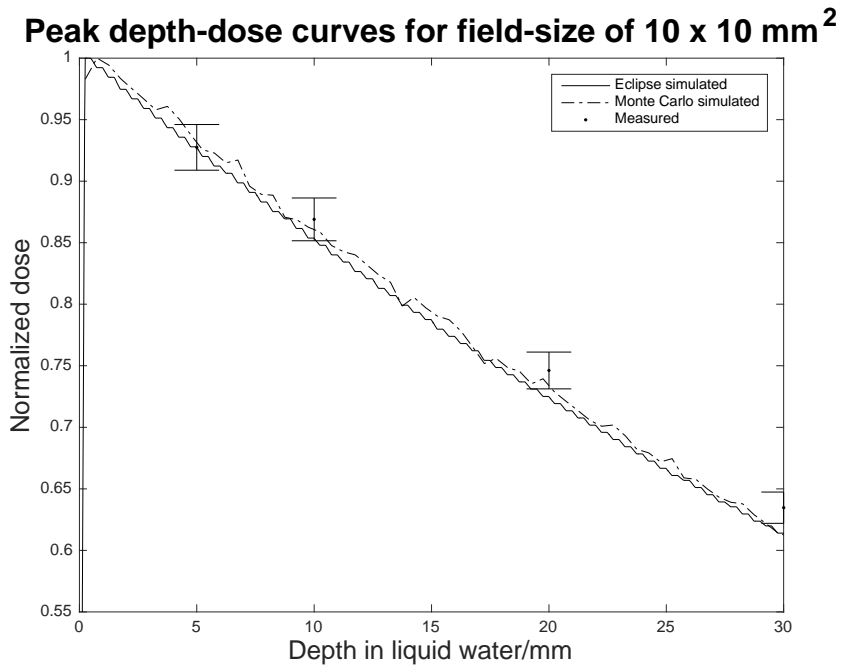
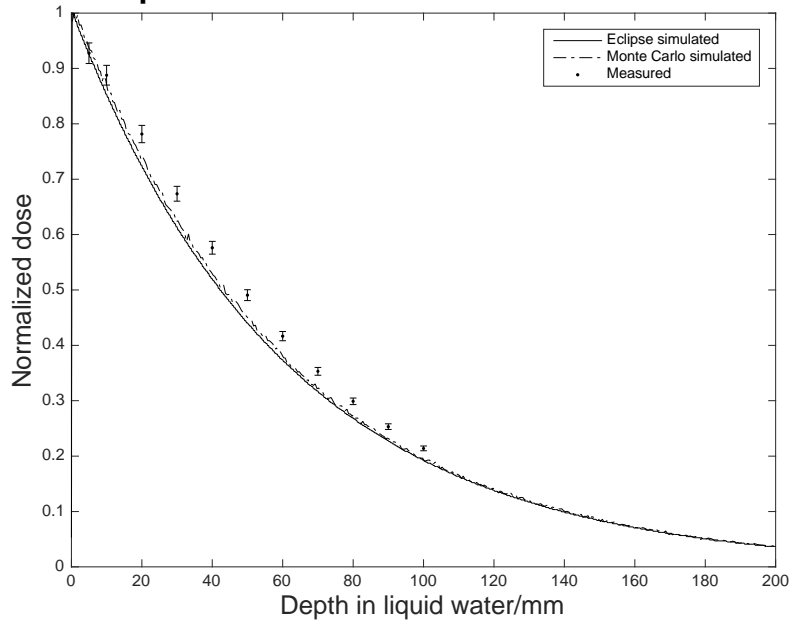


Figure 8 - Percentage Depth-Dose Curves for a $10 \times 10 \text{ mm}^2$ field of synchrotron peak-dose radiation incident on a $200 \times 200 \times 200 \text{ mm}^3$ liquid water phantom. The figure shows Eclipse-calculated data, Monte Carlo simulated data and data measured using a pinpoint ionization chamber. The Eclipse data and the Monte Carlo data are normalized to the maximum value of the data set and the measured data are normalized against the Eclipse data at 5 mm depth since the first measurement point was obtained at 5 mm depth. The figure shows both the entire water-phantom a), and an enlargement of the first 30 mm b). The error bars for the measured data represent a 2 % uncertainty of the measured values. The figure displays an excellent agreement between Eclipse-calculated and Monte Carlo simulated data and also a rather good agreement between the measured and the Eclipse-calculated data, were the calculated data mostly lies within the error bars of most measurement points.

a)

Peak depth-dose curves for field-size of $20 \times 20 \text{ mm}^2$



b)

Peak depth-dose curves for field-size of $20 \times 20 \text{ mm}^2$

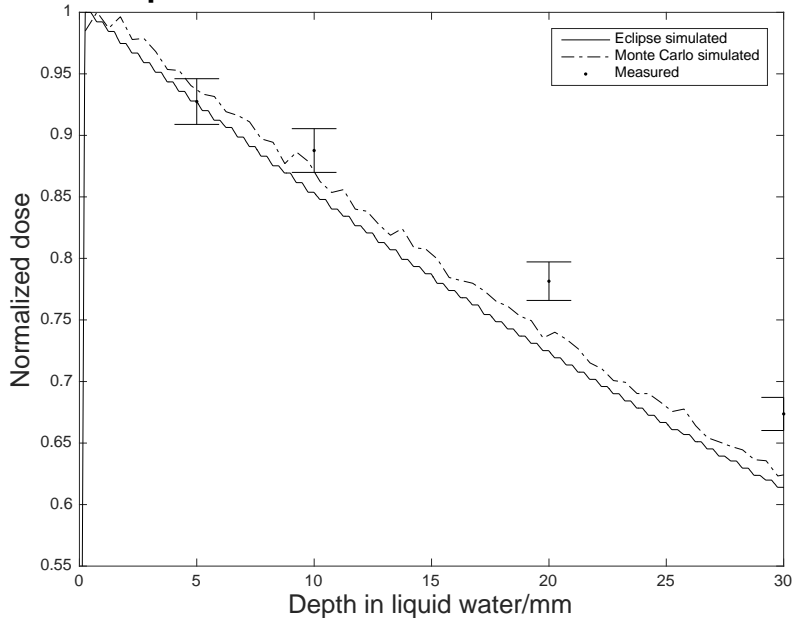
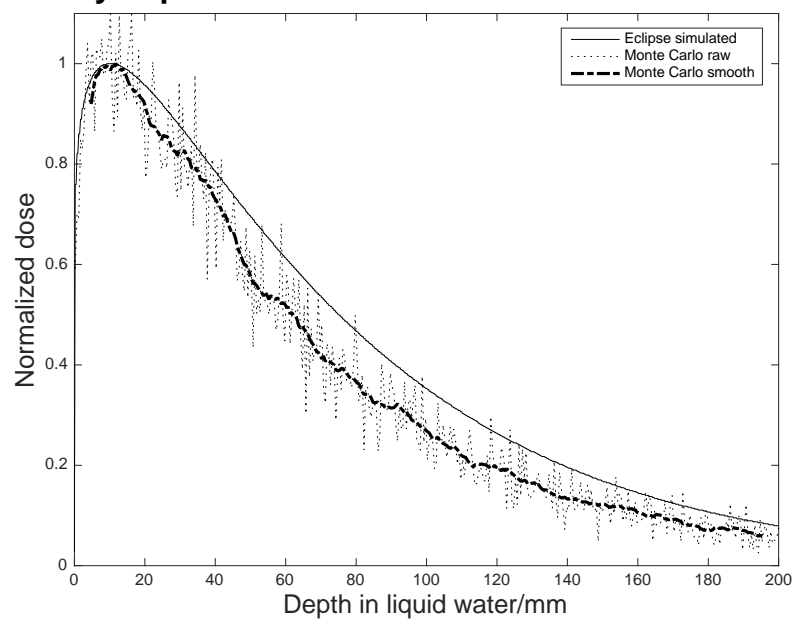


Figure 9 - Percentage Depth-Dose Curves for a $20 \times 20 \text{ mm}^2$ field of synchrotron peak-dose radiation incident on a $200 \times 200 \times 200 \text{ mm}^3$ water phantom. The figure shows Eclipse-calculated data, Monte Carlo simulated data and data measured using a pinpoint ionization chamber. The Eclipse data and the Monte Carlo data are normalized to the maximum value of the data set and the measured data are normalized against the Eclipse data at 5 mm depth since the first measurement point was obtained at 5 mm depth. The figure shows both the entire water-phantom a), and an enlargement of the first 30 mm b). The error bars for the measured data represent a 2 % uncertainty of the measured values. The Eclipse-calculated data seem to slightly underestimate the dose compared to the Monte Carlo simulated data and to the measured data.

Valley percentage depth dose curves in the water phantom are shown in Figure 10 to Figure 13. For the valley PDD curves no measurement data are shown since measurements were only performed on broad beam fields, and these measurements correspond to peak dose. The figures show that for the $10 \times 1 \text{ mm}^2$, $20 \times 1 \text{ mm}^2$ and $10 \times 10 \text{ mm}^2$ fields Eclipse overestimates the dose compared to Monte Carlo simulations. This overestimation increases as the field size decreases so that the overestimation is largest for the $10 \times 1 \text{ mm}^2$ field and smallest for the $10 \times 10 \text{ mm}^2$ field. For the $20 \times 20 \text{ mm}^2$ field Eclipse instead underestimates dose compared to Monte Carlo simulations.

a)

Valley depth-dose curves for field-size of $10 \times 1 \text{ mm}^2$



b)

Valley depth-dose curves for field-size of $10 \times 1 \text{ mm}^2$

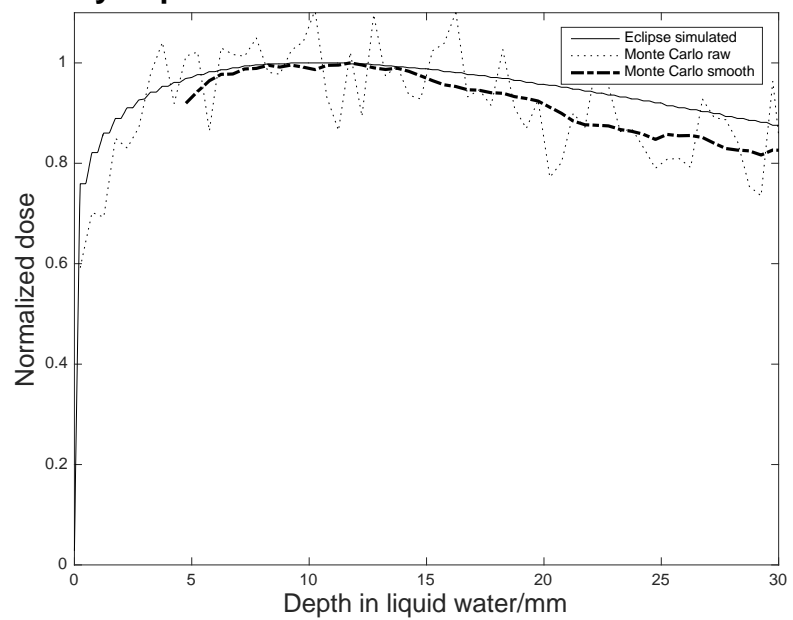
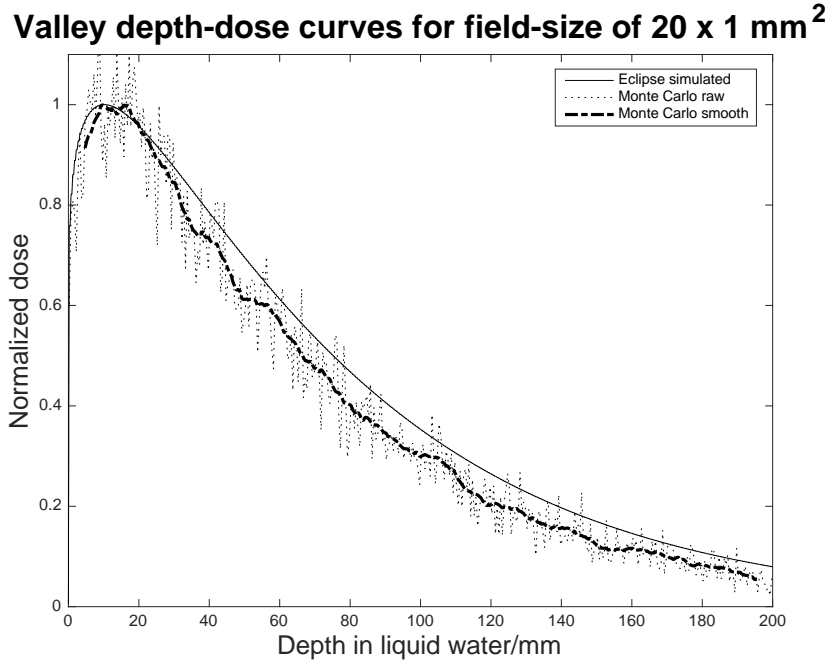


Figure 10 - Percentage Depth-Dose Curves for a $10 \times 1 \text{ mm}^2$ field of synchrotron valley-dose radiation incident on a $200 \times 200 \times 200 \text{ mm}^3$ liquid water phantom. The figure shows Eclipse-calculated data, Monte Carlo simulated raw data and smoothed Monte Carlo simulated data. The smoothed data has been averaged over 20 points using a moving average filter. The Eclipse calculated and the smoothed Monte Carlo data are normalized to the maximum value of the data set and the raw Monte Carlo data are normalized to the maximum value of the smoothed Monte Carlo data. The figure shows both the entire water-phantom a), and an enlargement of the first 30 mm b). Compared to the Monte Carlo simulations the Eclipse calculations are markedly overestimating the dose.

a)



b)

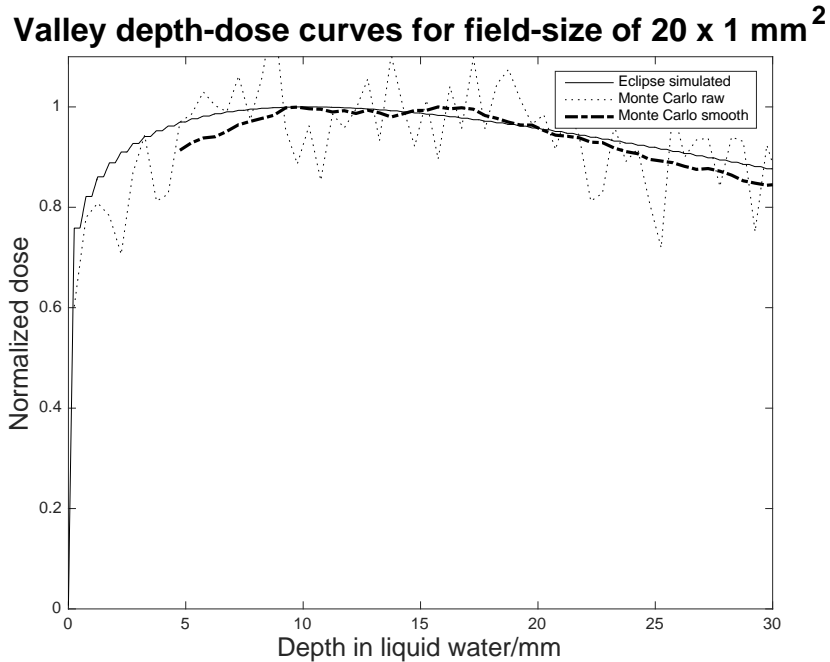
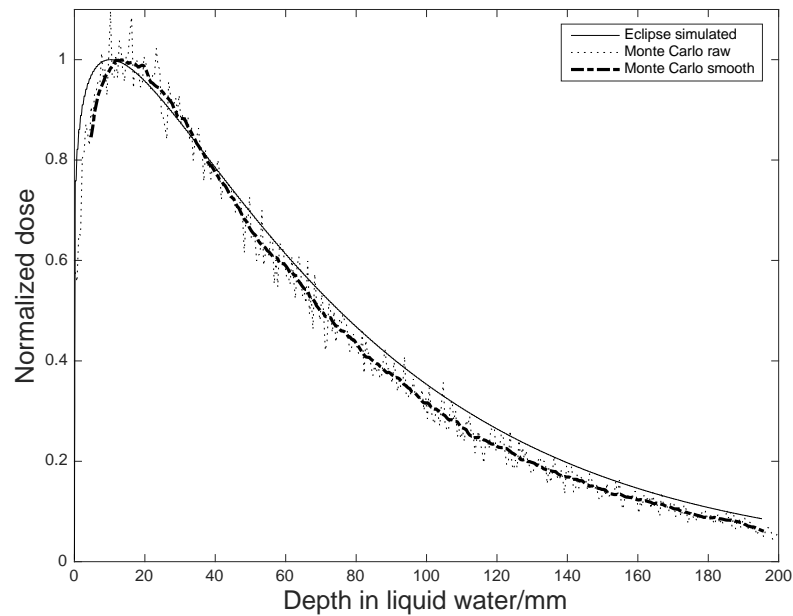


Figure 11 - Percentage Depth-Dose Curves for a $20 \times 1 \text{ mm}^2$ field of synchrotron valley-dose radiation incident on a $200 \times 200 \times 200 \text{ mm}^3$ liquid water phantom. The figure shows Eclipse-calculated data, Monte Carlo simulated raw data and smoothed Monte Carlo simulated data. The smoothed data has been averaged over 20 points using a moving average filter. A) The Eclipse calculated and the smoothed Monte Carlo data are normalized to the maximum value of the data set and the raw Monte Carlo data are normalized to the maximum value of the smoothed Monte Carlo data. The figure shows both the entire water-phantom a), and an enlargement of the first 30 mm b). Compared to the Monte Carlo simulations the Eclipse calculations are markedly overestimating the dose.

a)

Valley depth-dose curves for field-size of $10 \times 10 \text{ mm}^2$



b)

Valley depth-dose curves for field-size of $10 \times 10 \text{ mm}^2$

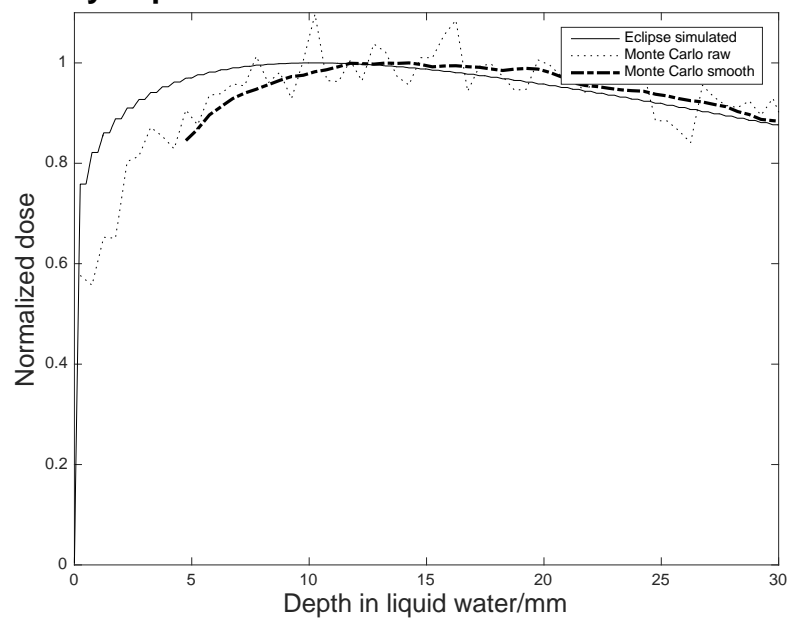
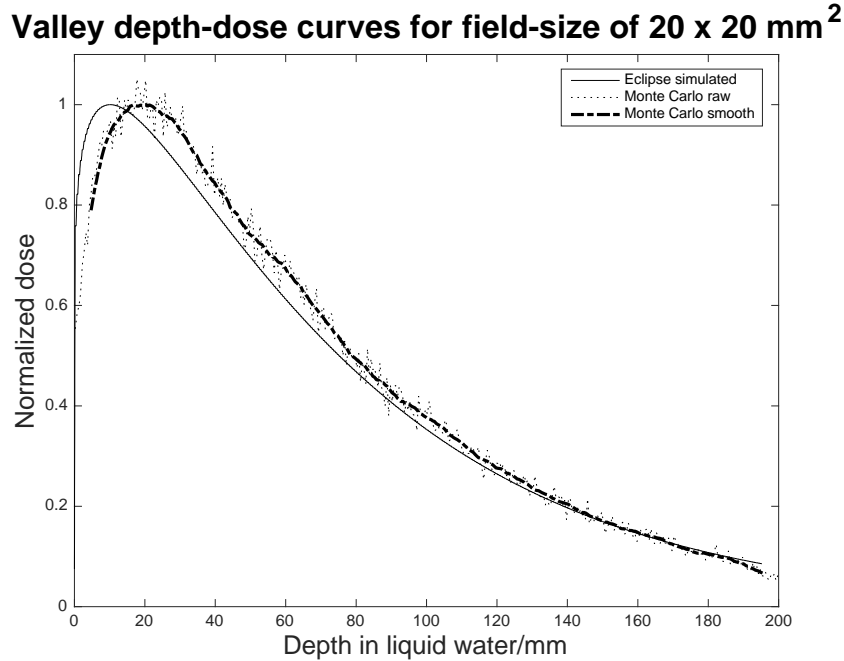


Figure 12 - Percentage Depth-Dose Curves for a $10 \times 10 \text{ mm}^2$ field of synchrotron valley-dose radiation incident on a $200 \times 200 \times 200 \text{ mm}^3$ liquid water phantom. The figure shows Eclipse-calculated data, Monte Carlo simulated raw data and smoothed Monte Carlo simulated data. The smoothed data has been averaged over 20 points using a moving average filter. The Eclipse-calculated and the smoothed Monte Carlo data are normalized to the maximum value of the data set and the raw Monte Carlo data are normalized to the maximum value of the smoothed Monte Carlo data. The figure shows both the entire water-phantom a), and an enlargement of the first 30 mm b). Compared to the Monte Carlo simulations the Eclipse calculations are slightly overestimating the dose.

a)



b)

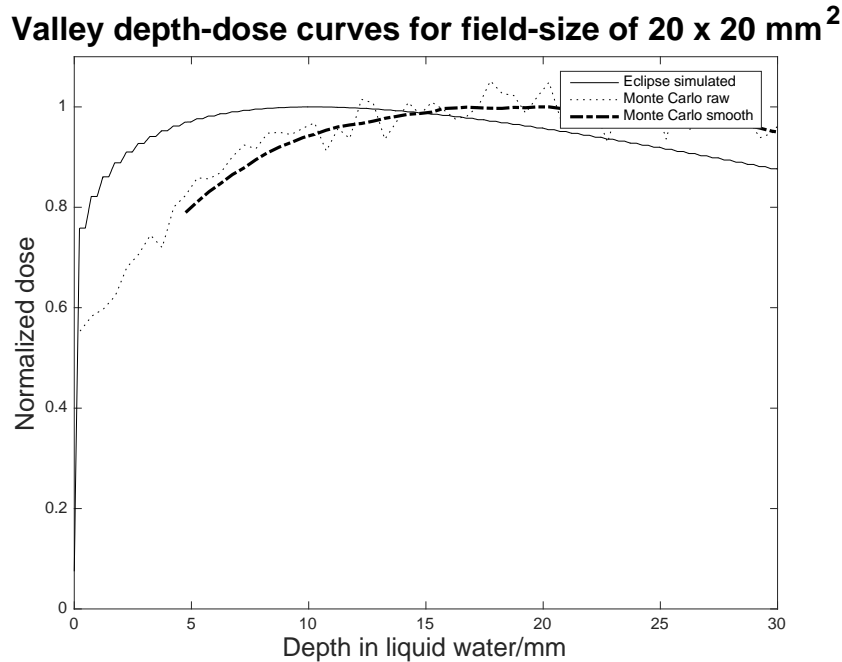
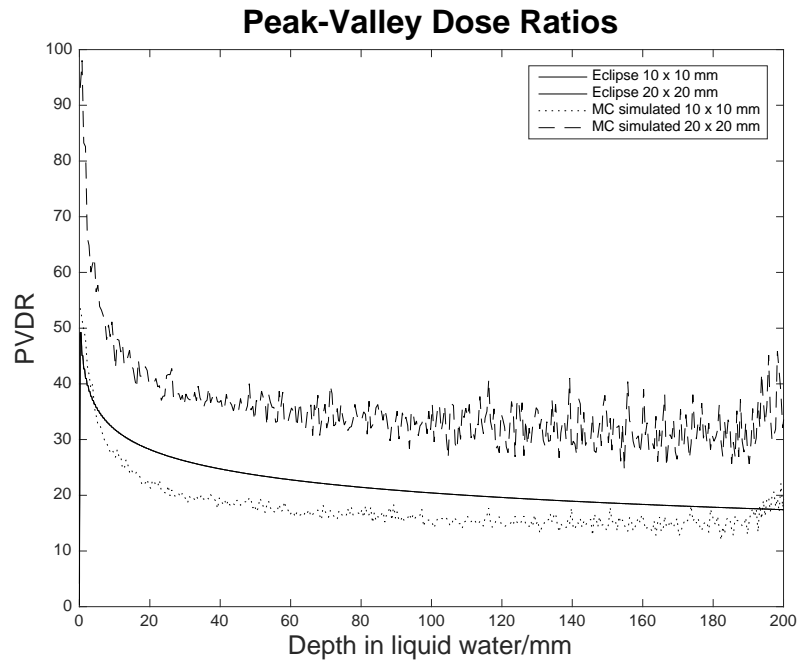


Figure 13 - Percentage Depth-Dose Curves for a $20 \times 20 \text{ mm}^2$ field of synchrotron valley-dose radiation incident on a $200 \times 200 \times 200 \text{ mm}^3$ liquid water phantom. The figure shows Eclipse-calculated data, Mont Carlo simulated raw data and smoothed Monte Carlo simulated data. The smoothed data has been averaged over 20 points using a moving average filter. The Eclipse-calculated and the smoothed Monte Carlo data are normalized to the maximum value of the data set and the raw Monte Carlo data are normalized to the maximum value of the smoothed Monte Carlo data. The figure shows both the entire water-phantom a), and an enlargement of the first 30 mm b). Compared to the Monte Carlo simulations, the Eclipse calculations are underestimating the dose.

Figure 14 shows Eclipse-calculated and Monte Carlo simulated PVDR curves for a 10×10 mm 2 and a 20×20 mm 2 field incident on the water phantom. The figure shows that while for the Monte Carlo simulated data the PVDR is less decreasing with depth for the 10×10 mm 2 than for the 20×20 mm 2 field, for the Eclipse-calculated data the PVDRs are identical for both field sizes. This illustrates a substantial problem in the current version of the algorithm.

a)



b)

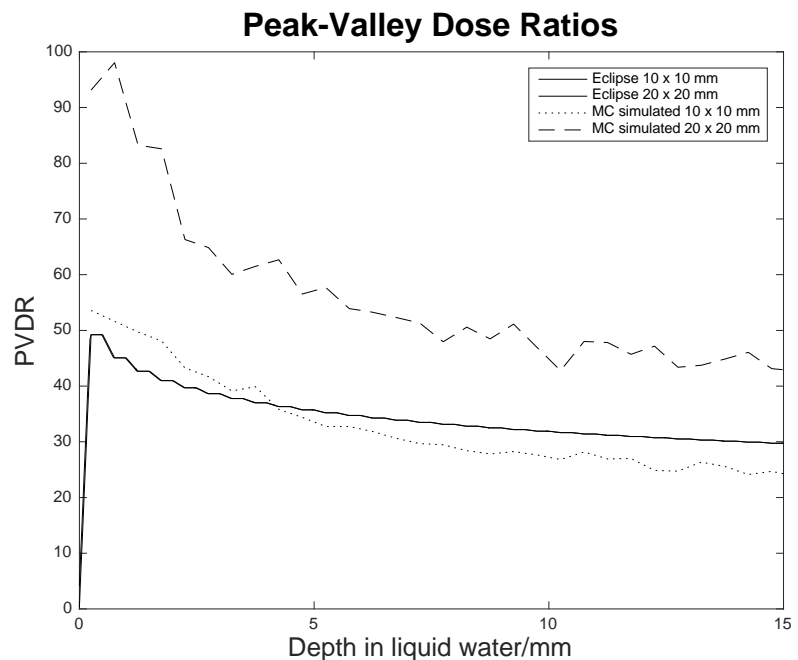


Figure 14 - Peak-valley dose ratios for a $10 \times 10 \text{ mm}^2$ and a $20 \times 20 \text{ mm}^2$ fields of synchrotron radiation incident on a $200 \times 200 \times 200 \text{ mm}^3$ liquid water phantom. The figure shows Eclipse-calculated data and Monte Carlo simulated data both for the entire water-phantom a), and an enlargement of the first 15 mm b). For the Monte Carlo simulated data, the PVDR is higher for the $10 \times 10 \text{ mm}^2$ field than for the $20 \times 20 \text{ mm}^2$ while for the Eclipse-calculated data, the PVDR is exactly the same for both field sizes, illustrating an important problem in the current version of the algorithm.

4.1.2 Field profiles

Figure 15 and Figure 16 shows Eclipse-calculated and measured field profiles at different depths for a $10 \times 10 \text{ mm}^2$ and a $20 \times 20 \text{ mm}^2$ field of synchrotron radiation orthogonally incident on a cubic $200 \times 200 \times 200 \text{ mm}^3$ water phantom. It is important to note that in these figures the measured data has been normalized to the calculated data at the depth at which measurements have been performed. Thus the measured data at 10 mm depth are normalized to the maximum of the Eclipse-calculated data at 10 mm depth and so on. Figure 15 illustrates how the center regions of the Eclipse-calculated profiles are completely straight whilst for the measured profile they are noisier. One may note how the measured horizontal field profiles, especially for the $20 \times 20 \text{ mm}^2$ field, has a somewhat rounded appearance. One may also deduce from these figures that, especially for the vertical field profiles, Eclipse fails to account for the penumbra at the field edges that, although small, is measured by the film.

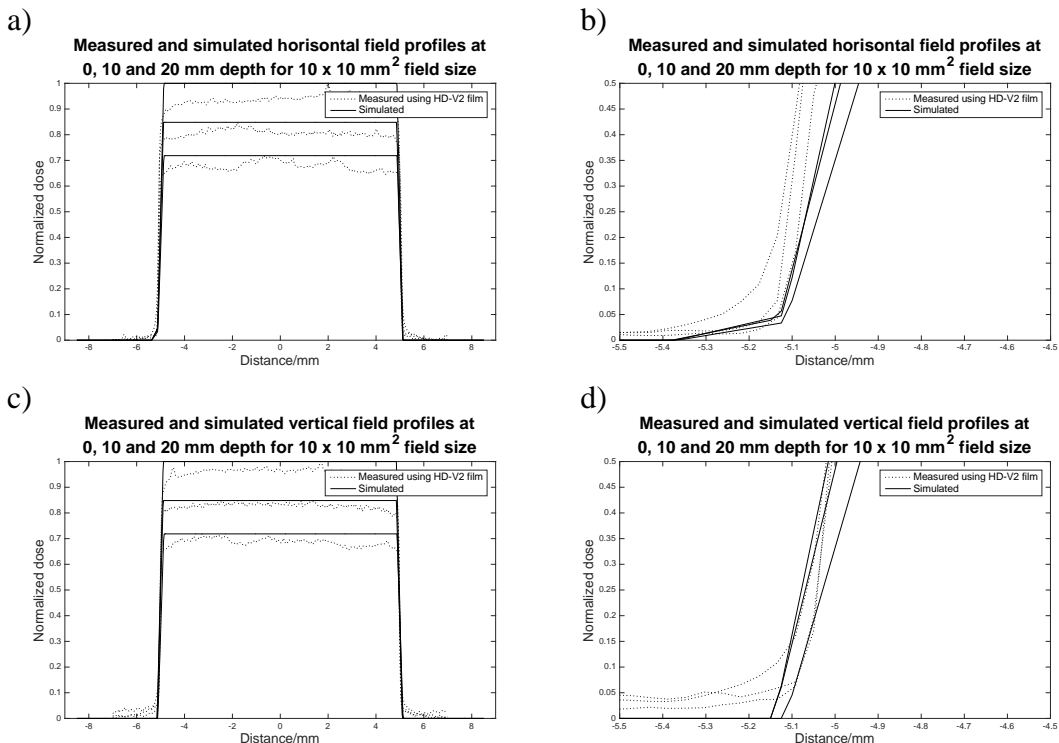


Figure 15 - Horizontal (a) and b)) and vertical (c) and d)) field profiles from a $10 \times 10 \text{ mm}^2$ field of synchrotron peak dose radiation incident on a $200 \times 200 \times 200 \text{ mm}^3$ liquid water phantom at 0 mm, 10 mm and 20 mm depth. The figure shows both Eclipse-calculated data and data measured using GafChromic HV-V2 film. The Eclipse data are normalized to the maximum of the data set maximum at 0 mm depth and the measured data are normalized against the maximum of the Eclipse data at the current depth. That is, the data measured at 10 mm are normalized to the maximum of the Eclipse-calculated data at 10 mm and so on.

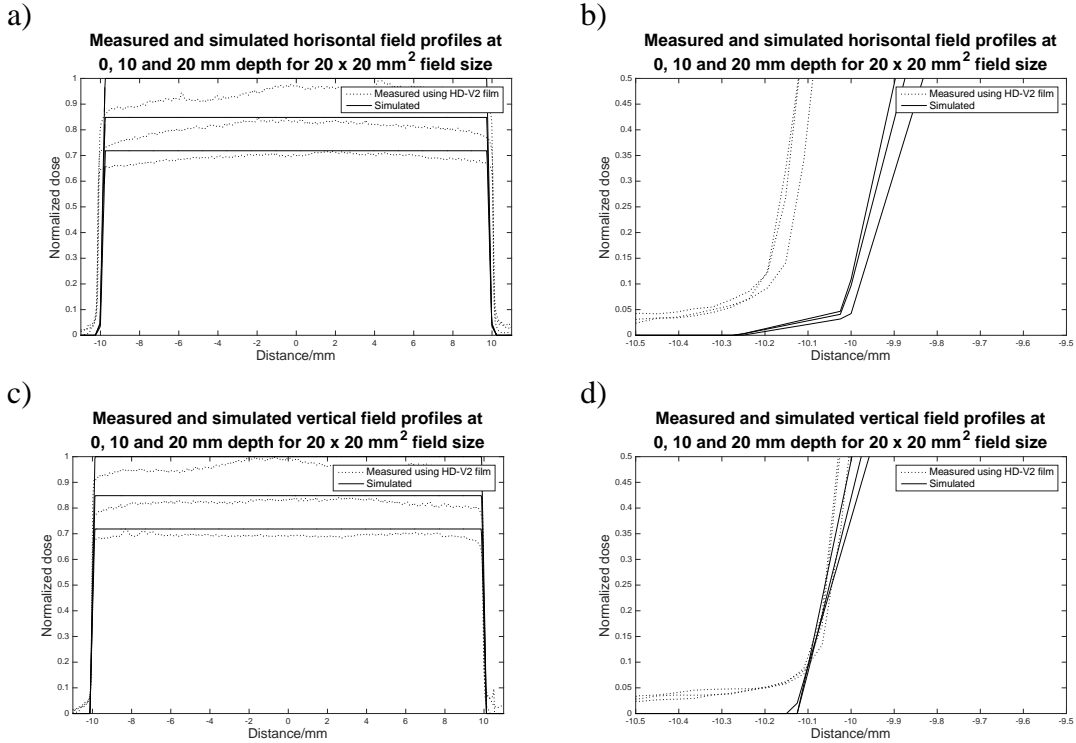


Figure 16 - Horizontal (a) and b)) and vertical (c) and d)) field profiles from a $20 \times 20 \text{ mm}^2$ field of synchrotron peak dose radiation incident on a $200 \times 200 \times 200 \text{ mm}^3$ liquid water phantom at 0 mm, 10 mm and 20 mm depth. The figure shows both Eclipse-calculated data and data measured using GafChromic HV-V2 film. The Eclipse data are normalized to the maximum of the data set at 0 mm depth and the measured data are normalized against the maximum of the Eclipse data at the current depth. That is, the data measured at 10 mm are normalized to the maximum of the Eclipse-calculated data at 10 mm and so on.

4.2 Inhomogeneous phantoms

The CT-values fed to Eclipse for the different slab materials used for creating the phantoms can be found in Table 2.

Table 2 – CT values of the different slab materials used to create the phantoms. The CT values were obtained by extracting the electron density to Hounsfield unit and the physical density to Hounsfield unit calibration curves from Eclipse and then using the known electron densities and physical densities of the slab materials to obtain CT values to plug into eclipse. Since one CT value was obtained from the electron density to Hounsfield unit calibration curve and one was obtained from the physical density to Hounsfield unit calibration curve, the stated CT values are averages over these two.

Phantom material	CT Value (HU)
Solid water (SW)	29
Lung equivalent (LE)	-704
Inner bone (IB)	143
Cortical bone (CB)	1378

Table 3 shows measured and Eclipse-calculated dose ratios between dose in the inhomogeneous phantom and in the solid water phantom. The agreement between calculated and measured dose ratios for the solid water phantom, bone phantom SCW phantom and CCW phantom is reasonably good. The calculated values are within or almost within the uncertainties of the measured ones. For the lung phantom however, the agreement is significantly worse. The calculated dose ratio strongly overestimates the measured value.

Table 3 – Eclipse-calculated and measured dose ratios between dose in tissue equivalent phantoms and dose in water. The construction of the phantoms can be found in Table 1.

Phantom	Measurement Depth /mm	DOSE RATIO	
		Calculated	Measured
Lung phantom	20	4.20	1.12 ± 0.03
Bone phantom	20	0.911	0.983 ± 0.027
SCW phantom	42	1.29	1.25 ± 0.04
CCW phantom	42	1.15	1.16 ± 0.03

Figure 17 shows Eclipse-calculated peak dose in the inhomogeneous phantoms described in the method section (Table 1). For the SCW phantom, the figure also includes Monte Carlo simulated data. Eclipse calculates high differences in deposited dose between lung, solid water and bone. When looking at the Eclipse data, the deposited dose seem to depend on CT value so that a higher CT value entails a larger dose deposition and vice versa. When comparing the Eclipse-calculated data to the Monte Carlo simulated data in image d) one can see that although the Monte Carlo simulated data show a somewhat smaller deposited dose in lung tissue than in solid water, the difference is not nearly as large as for the Eclipse-calculated data. This discrepancy between Eclipse-calculated and Monte Carlo simulated data suggests that there is an error in the algorithm.

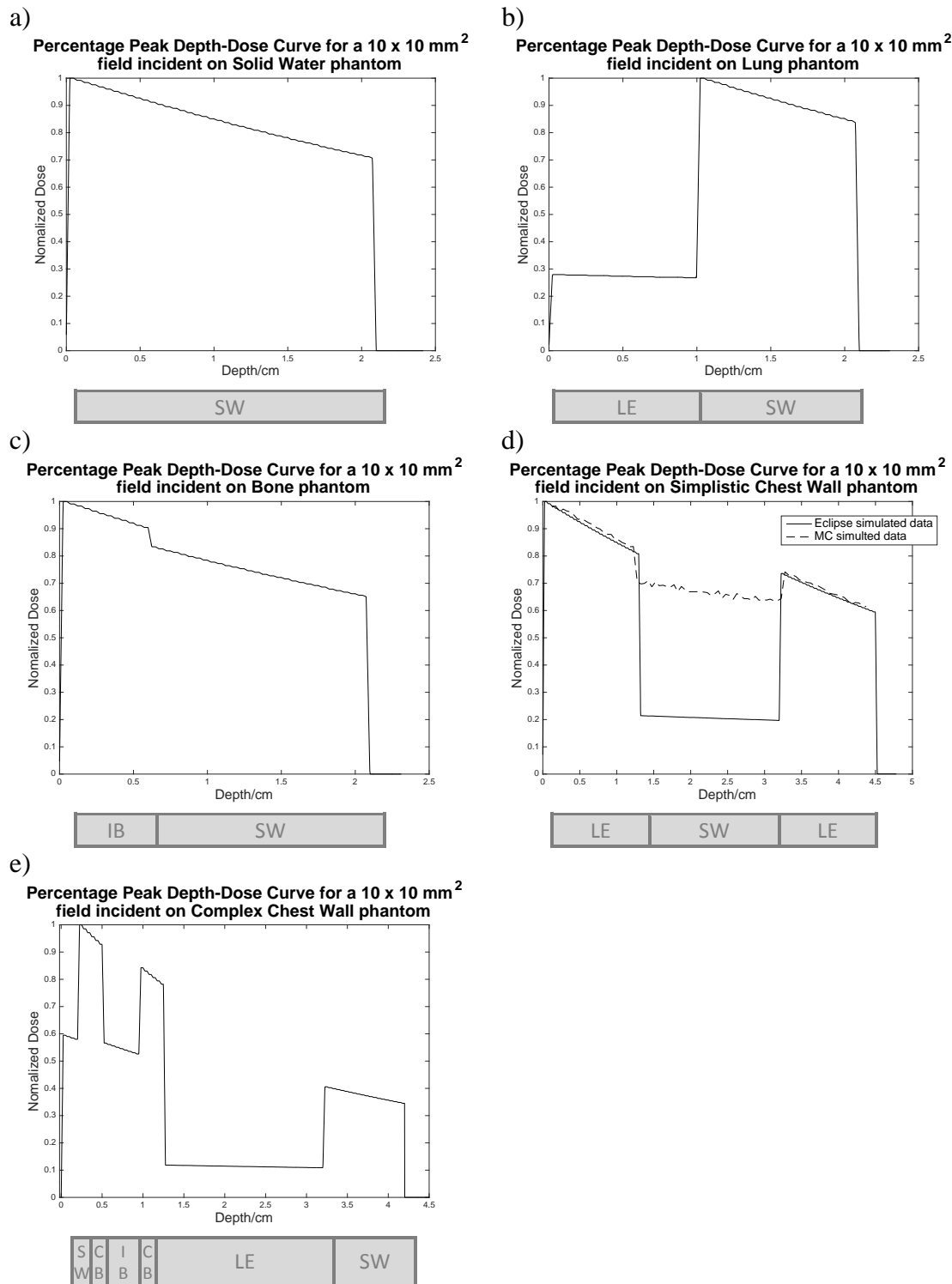


Figure 17 – Eclipse-calculated peak PDD curves for a $10 \times 10 \text{ mm}^2$ field of synchrotron radiation incident on inhomogeneous phantom constructed of GAMMEX solid water and tissue equivalent slabs. For the SCW phantom, data are also included from Monte Carlo simulations. The inserts under the diagrams show schematic images of the cross section geometry of the phantoms used. The construction of the phantoms can also be found in Table 1.

Figure 18 shows Eclipse-calculated valley dose in the inhomogeneous phantoms. Eclipse calculates relative dose depositions between the different materials similar to the ones for peak dose for the phantoms in image a), b) and c). In these images one can see the dose build up and drop-off effects in the intersections between materials with different HU. However in image d) and e) Eclipse does not calculate this. The dose drops to zero in the region where the dose deposition would be expected to be at its largest. This unexpected behavior suggests that there's an error somewhere in the code implemented in Eclipse, possibly related to the storing of the numbers in the calculated dose grid.

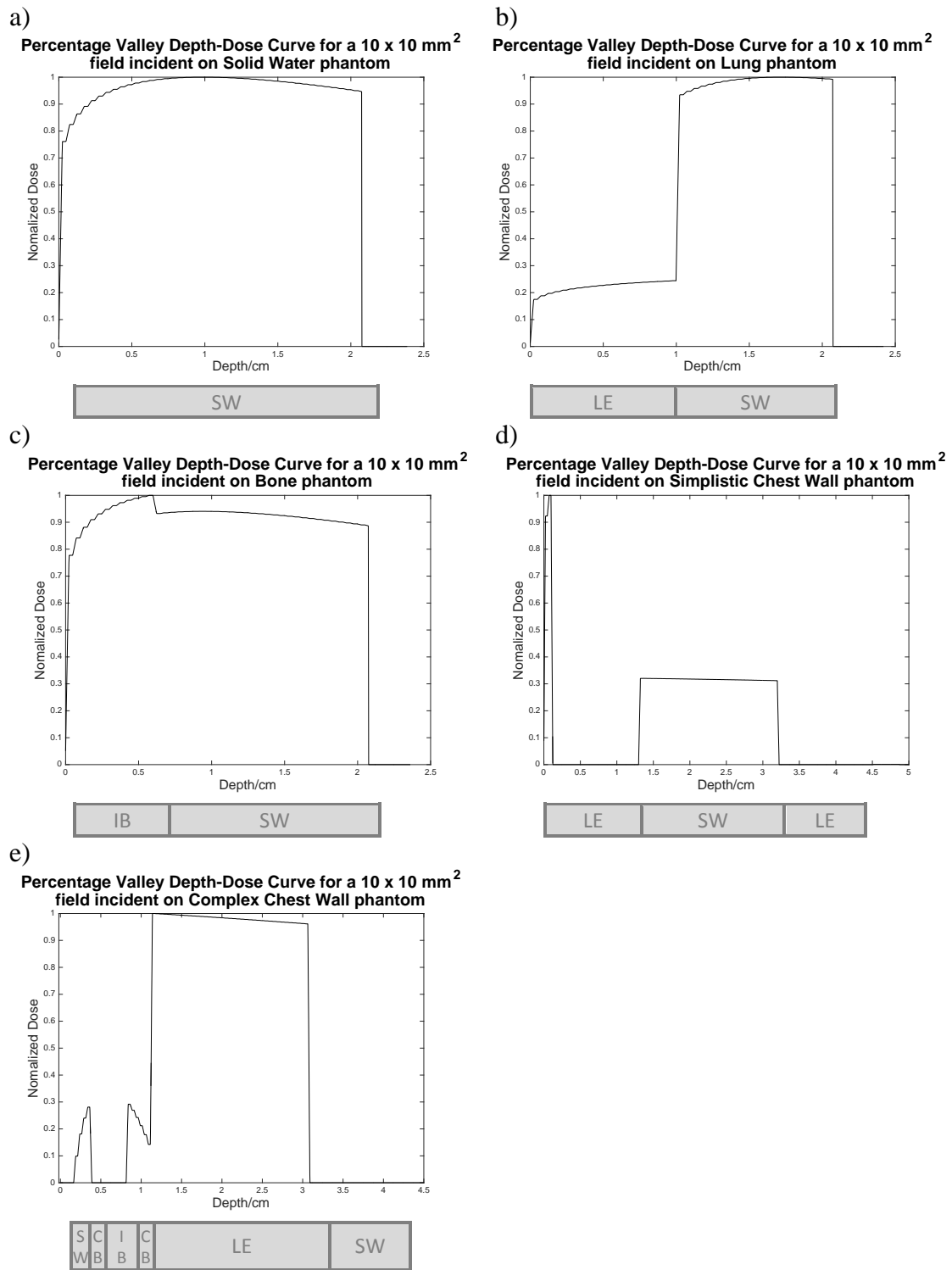


Figure 18 – Eclipse-calculated valley PDD curves for a $10 \times 10 \text{ mm}^2$ field of synchrotron radiation incident on inhomogeneous phantoms constructed of GAMMEX solid water and tissue equivalent slabs. The inserts under the diagrams show schematic images of the cross section geometry of the phantoms used. The construction of the phantoms can also be found in Table 1.

Figure 19 shows Eclipse-calculated PVDRs in the inhomogeneous phantoms. Eclipse seems to calculate more decreasing PVDR curve for materials with higher CT values and vice versa (compare to the CT-values in Table 2).

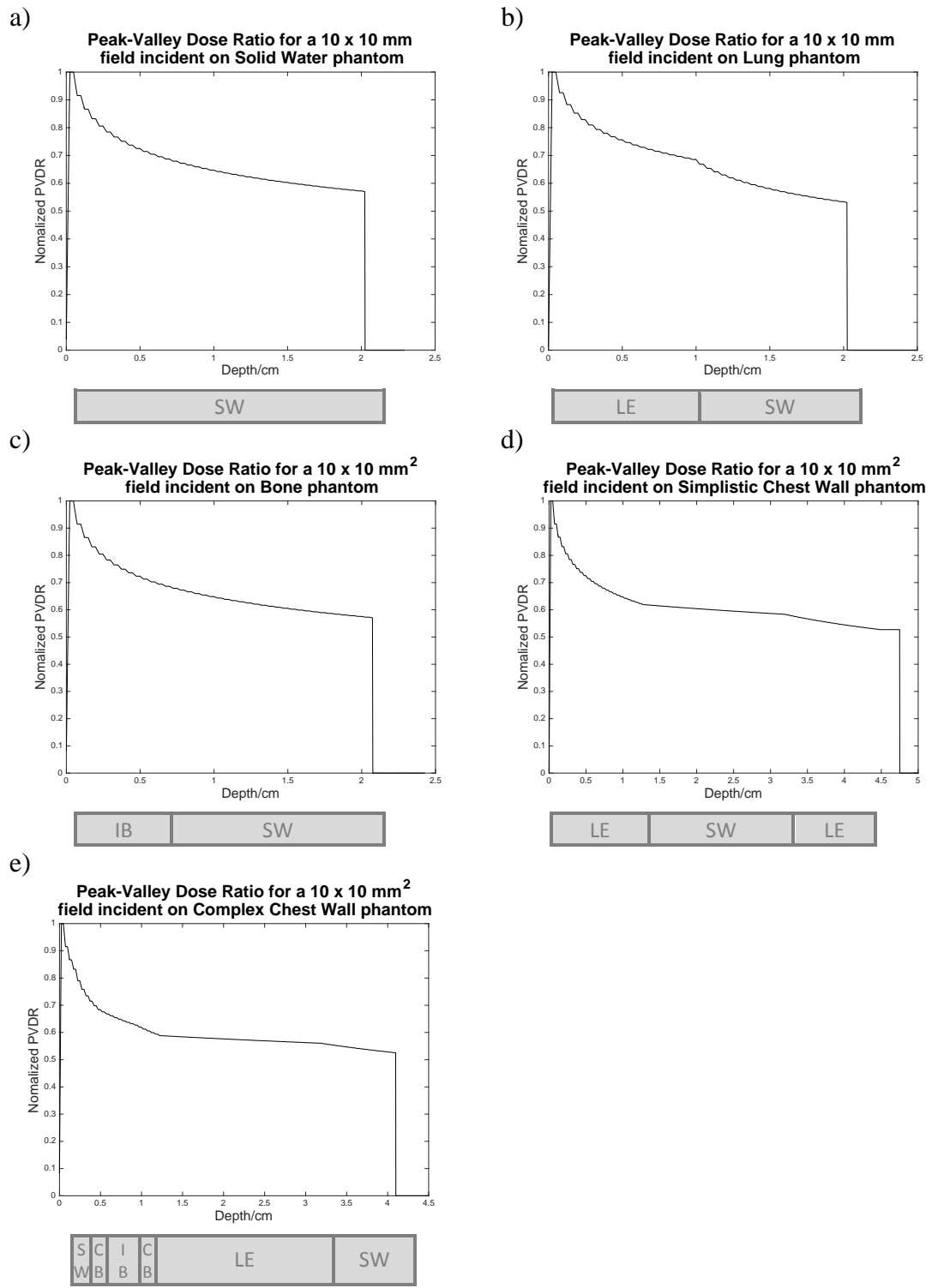


Figure 19 – Eclipse-simulated PVDRs for a $10 \times 10 \text{ mm}^2$ field of synchrotron radiation incident on inhomogeneous phantoms constructed of GAMMEX solid water and tissue equivalent slabs. The inserts under the diagrams show schematic images of the cross section geometry of the phantoms used. The construction of the phantoms can also be found in Table 1.

4.3 Obliquity

Table 4 shows calculated and measured dose ratios between doses at 35 mm depth in a solid water phantom for a field incident with an angle to the normal and for a field incident orthogonal to the phantom surface. The calculated and measured values follow the same trend, were the dose ratio decreases as the angle increases and all of the calculated values are within the error margin of the measured values.

Table 4 – Calculated and measured dose ratios between dose measured at 35 mm for a 10 x 10 mm² field of synchrotron radiation incident at obliquely on a phantom and dose measured for octagonal field direction. Two different phantoms have been used, one constituting of 50 mm solid water slabs and the other of 10 mm lung equivalent slabs and 40 mm solid water slabs.

Angle	50 mm SW		10 mm LE + 40 SW	
	Calculated	Measured	Calculated	Measured
5°	0.992	0.999 ± 0.028	0.999	0.999 ± 0.020
10°	0.991	0.992 ± 0.028	0.997	0.994 ± 0.020
20°	0.944	0.966 ± 0.027	0.977	0.973 ± 0.020

5 Discussion and Conclusion

The main findings of this work are: firstly, one may note that the algorithm in general predicts the peak PDD in homogeneous materials quite accurately, as can be seen in Figure 6 to Figure 9. The small deviations that exists constitutes of underestimations of dose for larger field sizes (the 10 × 10 mm² and the 20 × 20 mm² fields). These deviations could possibly be explained by the fact that the algorithm makes the approximation that peak dose is equal to primary dose. Thus it does not account for dose scattered from the valley regions into the peak region and the dose calculated by Eclipse would be slightly lower than the actual dose. Since the amount of scattered dose is larger for a larger field size, this underestimation would increase with field size.

Secondly, the agreement for valley PDD in homogeneous materials is not as good as the peak PDD. The dose calculated using Eclipse is smaller than the dose obtained through Monte Carlo simulations for smaller fields sizes (the 10 × 1 mm², 20 × 1 mm² and 10 × 10 mm²) and this deviation increases when field size decreases (see Figure 10 to Figure 12). For the 20 × 20 mm² field the dose calculated using Eclipse is instead larger than the dose obtained through Monte Carlo simulations (see Figure 13). An explanation for this may be found in Figure 14, which shows Eclipse and Monte Carlo simulated PVDRs for a 10 × 10 mm² and a 20 × 20 mm² field. In the Monte Carlo simulated data, the PVDR decreases more slowly with depth for the 10 × 10 mm² field than for the 20 × 20 mm² field, while for the Eclipse-calculated data the PVDRs are identical for both field sizes. Theoretically, a smaller field size would entail a more slowly decreasing PVDR since less radiation is scattered from the peaks into the valleys for a smaller field size. A limitation of this version of the Eclipse algorithm is however that it fails to calculate this field size dependence of the PVDRs. Since the valley dose in the Eclipse algorithm is obtained by dividing the peak dose with the PVDR, this limitation entails an error in the calculated valley dose.

Thirdly, Eclipse calculates field profiles in homogeneous materials reasonably well. This agreement can be seen in Figure 15 and Figure 16, which shows calculated and film-measured profiles. One discrepancy that however exists is noticeable in the vertical field profile for the 20 × 20 mm² field. The measured profiles show a somewhat rounded appearance that cannot

be seen in the measured profile. This can be explained by something referred to in synchrotron science as the beam ‘roll-off’ effect.

The IMBL front-end has two primary, high heatload copper slits defining the beam in the horizontal and vertical direction. These slits are *in vacuo* and are approximately 13.85 m downstream of the wiggler. For MRT studies, the horizontal opening is approximately 12 mm and the vertical opening 0.6 mm (well defined). The larger, horizontal beam defining slit entails a larger beam divergence of 5.0 mrad compared to 0.3 mrad in the vertical direction. This is a consequence of the fact that at relativistic radially accelerated energies electrons irradiate electromagnetic waves in a pattern that is sharply peaked in the direction of the motion of the electrons (Winick and Doniach, 1980). The beam divergence gives the dose-profiles a rounded look. This effect is referred to as the beam roll-off effect and represents the non-uniformity in the field profile. The beam roll off effect is much more pronounced for the horizontal dose profiles than for the vertical dose profiles, and moreover it increases with larger field sizes (Crosbie, 2008, Stevenson et al., 2012).

In the simple pencil beam algorithm that Eclipse uses to calculate dose, this roll-off effect is not included at all. Thus it cannot be seen in the calculated data. In addition, the synchrotron radiation produced by a wiggler insertion device is polarized in the horizontal direction; a phenomenon also not accounted for in the Eclipse algorithm.

Fourthly, regarding dose calculations in inhomogeneous materials; the peak PDD curves for the inhomogeneous phantoms can be found in Figure 17. They show that the deposited dose is markedly larger in cortical bone and smaller in lung tissue compared to solid water. At first sight, these profiles looked surprising. From the NIST tables for the mass energy absorption coefficient, μ_{en}/ρ , cortical bone has $\mu_{en}/\rho = 0.04585 \text{ g/cm}^3$ and water $\mu_{en}/\rho = 0.02546 \text{ g/cm}^3$ at 100 keV. Thus cortical bone absorbs more energy per unit mass than water, which can explain why the deposited dose is higher in cortical bone than in water. For lung tissue however, $\mu_{en}/\rho = 0.02550 \text{ g/cm}^3$ at 100 keV which is quite similar to solid water and suggests that the absorbed dose would be fairly similar in lung and in water (NIST, 2004).

This is also consistent with the results of Company and Allen in their work from 1998 where they used the ESG4 Monte Carlo code to calculate dose distributions in a tissue-lung-tissue phantom. They obtained PDD that were slightly more decreasing with depth for tissue than for lung, but where the absorbed dose was quite similar in both lung and soft tissue. In the PDD curves generated in their work you did not see the drop in dose at the intersections between materials that can be seen in Figure 17 (Company and Allen, 1998).

To investigate whether the dose distribution calculated by Eclipse was correct or not, a Monte Carlo simulation performed to obtain dose in the SCW phantom. The Monte Carlo simulated data can be shown in Figure 17 d). Although this data show a slightly smaller dose deposition in lung tissue than in solid water, the discrepancy is not nearly as large as in the Eclipse-calculated data. This suggests that there’s an error in the algorithm that comes to show when calculating dose in certain materials. It should be noted that when the Eclipse calculated data was compared to Monte Carlo simulated data of energy per voxel, the agreement was very good. Thus, a possible explanation to this discrepancy is that Eclipse might fail to correctly take into account the density of the medium.

For the valley dose, Eclipse performs similar as for peak dose the solid water, lung and bone phantoms in Figure 18 a), b) and c). For the SCW and CCW phantoms however, the dose inexplicably drops to zero in the regions of the phantom where you would expect it to have a maximum. Looking at the PVDR in Figure 19, they seem to be correct, with more decreasing

PVDRs for materials with higher CT values. Thus, the unexpected behavior of the valley PDDs cannot be explained by an error in the PVDR. Instead, it seems to be due to a bug in the code, possibly related to the storing of the numbers in the calculated dose grid. This bug is an important finding since, if left unnoticed it could have resulted in erroneous plans and possibly inaccurate patient treatments. It should thus be considered an important discovery of the work.

Lastly, the limited data available for oblique field (Table 4) suggest that Eclipse handles Oblique fields rather well.

The data presented in this work is the first of its kind. The implementation of this algorithm in Eclipse is the first effort made to create a calculation engine for MRT in a commercially available TPS and this report presents the first data from this TPS. When looking at these data, it is important to be aware of the fact that the algorithm is still a work in progress. The work presented in this essay should be considered a step on the path towards creating a clinically viable TPS for MRT, not a presentation of a complete solution. With that in mind, the presented data are encouraging and could, with further improvements, be put to important clinical use.

Other efforts involving creation and validation of TPSs for MRT include the work by Martinez-Rovira *et al.* from 2012 that consisted of the creation of a Monte Carlo based dose calculation engine for MRT treatment planning. To test their calculation engine, Martinez-Rovira *et al.* simulated irradiations on inhomogeneous phantoms created of solid water and cortical bone equivalent slabs to mimic the human skull. The same phantoms were irradiated while point doses were measured at different depths in the phantoms using radiochromic film. They found that measured and simulated doses agreed within the calculated uncertainties. However, all of their measurements were on axis and only point dose measurements were taken. Thus, their validation could have been expanded by including for example field profiles (Martinez-Rovira *et al.*, 2012).

One should keep in mind that Monte Carlo simulations are more accurate than analytical dose calculation methods, thus one can expect a better agreement between simulated and measured data with Monte Carlo simulations than for an analytical method. The downside with Monte Carlo simulations though, is that they are a lot more time consuming than analytical methods. To calculate dose over a CT data set of a dog head phantom with the calculation engine of Martinez-Rovira *et al.* took slightly less than a day to perform. This is quite long if you want to be able to recalculate the dose grid a couple of times while creating a plan. The calculation engine was also never incorporated in a GUI, which is something that realistically and practically needs to be done before it can be implemented in a clinical environment (Martinez-Rovira *et al.*, 2012).

Bartzsch suggested an analytical approach to the problem of treatment planning in MRT in his PhD thesis work from 2014. He used a kernel-based technique to calculate both peak and valley dose from the fluence pattern of the incident radiation. For validation purposes, calculated doses were never compared to measured data, only to Monte Carlo simulations, because the author argued that Monte Carlo simulations are the most accurate dose calculation methods and because the Monte Carlo code used was separately validated against measurements (Bartzsch, 2014).

To validate the dose calculations, Bartzsch compared Monte Carlo simulated and calculated PDD curves and field profiles at different depths in a homogeneous water phantom and in an anthropomorphic head phantom. He found that the agreement was rather good for peak dose, but that the method was struggling to calculate valley dose correctly (Bartzsch, 2014). Thus,

there might be need for a different approach when it comes to calculating valley dose in a reasonable amount of time, such as the one presented in the work of Poole *et al.*

Before a clinical implementation of the TPS can be made possible, it is crucial to benchmark calculated absolute doses against measurements. A limitation to this work is that it only presents relative dose data. Whilst useful to get an idea of the general performance of the TPS, it is very important to also investigate whether the absolute doses (in Gray) the algorithm calculates are correct.

The next step would then be to start generating actual treatment plans using CT-data as input. To be able to compare plans generated with this TPS to conventional treatment plans would be very valuable when investigating the benefits of MRT in comparison to conventional radiotherapy.

Being able to use Eclipse interface when implementing a TPS for MRT in the clinic would be very valuable. Due to the widespread use of the Eclipse TPS, it is already known to a great deal of the staff working in radiotherapy today. Therefore, if the Eclipse interface could be used for treatment planning for MRT, it would facilitate the implementation processes because staff members wouldn't have to be educated in the usage of a new TPS. MRT would more easily be considered part of the already existing clinical workflow. This would entail that MRT could be used to treat patients sooner.

To conclude, the data obtained from the MRT calculation engine from Poole *et al.* is overall encouraging. Although it shows that there's still work to be done, these data hint that with further improvements there are great possibilities for this calculation engine to be implemented in the clinic in the future

6 References

- AHNESJO, A. & ASPRADAKIS, M. M. 1999. Dose calculations for external photon beams in radiotherapy. *Phys Med Biol*, 44, R99-155.
- ANDERSON, D., SIEGBAHN, E. A., FALLONE, B. G., SERDUC, R. & WARKENTIN, B. 2012. Evaluation of dose-volume metrics for microbeam radiation therapy dose distributions in head phantoms of various sizes using Monte Carlo simulations. *Phys Med Biol*, 57, 3223-48.
- ASHLAND. *GafChromic Dosimetry media, type HD-V2* [Online]. <http://www.ashland.com/search?q=HD-V2>.
- BARTZSCH, S. 2014. *Microbeam Radiation Therapy – physical and biological aspects of a new cancer therapy and development of a treatment planning system*.
- BARTZSCH, S., LERCH, M., PETASECCA, M., BRAUER-KRISCH, E. & OELFKE, U. 2014. Influence of polarization and a source model for dose calculation in MRT. *Med Phys*, 41, 041703.
- BOUCHET, A., LEMASSON, B., CHRISTEN, T., POTEZ, M., ROME, C., COQUERY, N., LE CLECH, C., MOISAN, A., BRAUER-KRISCH, E., LEDUC, G., REMY, C., LAISSLUE, J. A., BARBIER, E. L., BRUN, E. & SERDUC, R. 2013. Synchrotron microbeam radiation therapy induces hypoxia in intracerebral gliosarcoma but not in the normal brain. *Radiother Oncol*, 108, 143-8.
- BOUCHET, A., LEMASSON, B., LE DUC, G., MAISIN, C., BRAUER-KRISCH, E., SIEGBAHN, E. A., RENAUD, L., KHALIL, E., REMY, C., POILLOT, C., BRAVIN, A., LAISSLUE, J. A., BARBIER, E. L. & SERDUC, R. 2010. Preferential effect of synchrotron microbeam radiation therapy on intracerebral 9L gliosarcoma vascular networks. *Int J Radiat Oncol Biol Phys*, 78, 1503-12.

- BOUCHET, A., SERDUC, R., LAISSE, J. A. & DJONOV, V. 2015. Effects of microbeam radiation therapy on normal and tumoral blood vessels. *Phys Med*, 31, 634-41.
- BOYLAN, C. J.,AITKENHEAD, A. H., ROWBOTTOM, C. G. & MACKAY, R. I. 2013. Simulation of realistic linac motion improves the accuracy of a Monte Carlo based VMAT plan QA system. *Radiother Oncol*, 109, 377-83.
- CEBERG, C. P., BJARNGARD, B. E. & ZHU, T. C. 1996. Experimental determination of the dose kernel in high-energy x-ray beams. *Med Phys*, 23, 505-11.
- COMPANY, F. Z. & ALLEN, B. J. 1998. Calculation of microplanar beam dose profiles in a tissue/lung/tissue phantom. *Phys Med Biol*, 43, 2491-501.
- CORNELIUS, I., GUATELLI, S., FOURNIER, P., CROSBIE, J. C., SANCHEZ DEL RIO, M., BRAUER-KRISCH, E., ROSENFIELD, A. & LERCH, M. 2014. Benchmarking and validation of a Geant4-SHADOW Monte Carlo simulation for dose calculations in microbeam radiation therapy. *J Synchrotron Radiat*, 21, 518-28.
- CROSBIE, J. 2008. Synchrotron Microbeam Radiation Therapy. *PhD thesis* Monash University, Australia.
- CROSBIE, J. C., ANDERSON, R. L., ROTHKAMM, K., RESTALL, C. M., CANN, L., RUWANPURA, S., MEACHEM, S., YAGI, N., SVALBE, I., LEWIS, R. A., WILLIAMS, B. R. & ROGERS, P. A. 2010. Tumor cell response to synchrotron microbeam radiation therapy differs markedly from cells in normal tissues. *Int J Radiat Oncol Biol Phys*, 77, 886-94.
- CROSBIE, J. C., SVALBE, I., MIDGLEY, S. M., YAGI, N., ROGERS, P. A. & LEWIS, R. A. 2008. A method of dosimetry for synchrotron microbeam radiation therapy using radiochromic films of different sensitivity. *Phys Med Biol*, 53, 6861-77.
- CURTIS, H. J. 1967. The use of deuteron microbeam for simulating the biological effects of heavy cosmic-ray particles. *Radiat Res Suppl*, 7, 250-7.
- DAY, L. 2015. *A Geant4 Simulation of the Imaging and Medical Beamline at the Australian Synchrotron: Predicting Dosimetric Parameters of Interest for Microbeam Radiotherapy*. Master of Medical Physics, RMIT.
- DEVIC, S., TOMIC, N. & LEWIS, D. 2016. Reference radiochromic film dosimetry: Review of technical aspects. *Phys Med*, 32, 541-56.
- DILMANIAN, F. A., BUTTON, T. M., LE DUC, G., ZHONG, N., PENA, L. A., SMITH, J. A., MARTINEZ, S. R., BACARIAN, T., TAMMAM, J., REN, B., FARMER, P. M., KALEF-EZRA, J., MICCA, P. L., NAWROCKY, M. M., NIEDERER, J. A., RECKSIEK, F. P., FUCHS, A. & ROSEN, E. M. 2002. Response of rat intracranial 9L gliosarcoma to microbeam radiation therapy. *Neuro Oncol*, 4, 26-38.
- DILMANIAN, F. A., MORRIS, G. M., ZHONG, N., BACARIAN, T., HAINFELD, J. F., KALEF-EZRA, J., BREWINGTON, L. J., TAMMAM, J. & ROSEN, E. M. 2003. Murine EMT-6 carcinoma: high therapeutic efficacy of microbeam radiation therapy. *Radiat Res*, 159, 632-41.
- DILMANIAN, F. A., QU, Y., FEINENDEGEN, L. E., PENA, L. A., BACARIAN, T., HENN, F. A., KALEF-EZRA, J., LIU, S., ZHONG, Z. & MCDONALD, J. W. 2007. Tissue-sparing effect of x-ray microplanar beams particularly in the CNS: is a bystander effect involved? *Exp Hematol*, 35, 69-77.
- FOURNIER, P., CORNELIUS, I., CROSBIE, J., BERKVENS, P., DIPUGLIA, A., ROBERTS, N., REQUARDT, H., STEVENSON, A., HALL, C. J., PETASECCA, M., ROSENFIELD, A., BRAUER-KRISCH, E. & LERCH, M. 2014. Improving dosimetry for synchrotron Microbeam Radiation Therapy. *Electronic Presentation Online System*.
- LAISSE, J. A., BARTZSCH, S., BLATTMANN, H., BRAUER-KRISCH, E., BRAVIN, A., DALLERY, D., DJONOV, V., HANSON, A. L., HOPEWELL, J. W., KASER-HOTZ, B., KEYRILAINEN, J., LAISSE, P. P., MIURA, M., SERDUC, R., SIEGBAHL, A. E. & SLATKIN, D. N. 2013. Response of the rat spinal cord to X-ray microbeams. *Radiother Oncol*, 106, 106-11.

- MARTINEZ-ROVIRA, I., SEMPAU, J., FERNANDEZ-VAREA, J. M., BRAVIN, A. & PREZADO, Y. 2010. Monte Carlo dosimetry for forthcoming clinical trials in x-ray microbeam radiation therapy. *Phys Med Biol*, 55, 4375-88.
- MARTINEZ-ROVIRA, I., SEMPAU, J. & PREZADO, Y. 2012. Monte Carlo-based treatment planning system calculation engine for microbeam radiation therapy. *Med Phys*, 39, 2829-38.
- NETTELBECK, H., TAKACS, G. J., LERCH, M. L. & ROSENFELD, A. B. 2009. Microbeam radiation therapy: a Monte Carlo study of the influence of the source, multislit collimator, and beam divergence on microbeams. *Med Phys*, 36, 447-56.
- NIST 2004. X-Ray Mass Attenuation Coefficients. *National Institute of Standards and Technology*. <http://physics.nist.gov/PhysRefData/XrayMassCoef/tab4.html>.
- ORION, I., ROSENFELD, A. B., DILMANIAN, F. A., TELANG, F., REN, B. & NAMITO, Y. 2000. Monte Carlo simulation of dose distributions from a synchrotron-produced microplanar beam array using the EGS4 code system. *Phys Med Biol*, 45, 2497-508.
- POOLE, C., DAY, L., ROGERS, P. & CROSBIE, J. 2015. A treatment planning system for microbeam radiotherapy. *Unpublished*.
- PTW. 2012. *PTW detectors for small field dosimetry* [Online]. <http://www.ptw.de>.
- REGNARD, P., LE DUC, G., BRAUER-KRISCH, E., TROPRES, I., SIEGBAHLN, E. A., KUSAK, A., CLAIR, C., BERNARD, H., DALLERY, D., LAISSUE, J. A. & BRAVIN, A. 2008. Irradiation of intracerebral 9L gliosarcoma by a single array of microplanar x-ray beams from a synchrotron: balance between curing and sparing. *Phys Med Biol*, 53, 861-78.
- SCHNEIDER, U., PEDRONI, E. & LOMAX, A. 1996. The calibration of CT Hounsfield units for radiotherapy treatment planning. *Phys Med Biol*, 41, 111-24.
- SIEGBAHLN, E. A., STEPANEK, J., BRAUER-KRISCH, E. & BRAVIN, A. 2006. Determination of dosimetric quantities used in microbeam radiation therapy (MRT) with Monte Carlo simulations. *Med Phys*, 33, 3248-59.
- SLATKIN, D. N., SPANNE, P., DILMANIAN, F. A. & SANDBORG, M. 1992. Microbeam radiation therapy. *Med Phys*, 19, 1395-400.
- SPIGA, J., SIEGBAHLN, E. A., BRAUER-KRISCH, E., RANDACCIO, P. & BRAVIN, A. 2007. The GEANT4 toolkit for microdosimetry calculations: application to microbeam radiation therapy (MRT). *Med Phys*, 34, 4322-30.
- STEVENSON, A. W., HALL, C. J., MAYO, S. C., HAUSERMANN, D., MAKSIMENKO, A., GUREYEV, T. E., NESTERETS, Y. I., WILKINS, S. W. & LEWIS, R. A. 2012. Analysis and interpretation of the first monochromatic X-ray tomography data collected at the Australian Synchrotron Imaging and Medical beamline. *J Synchrotron Radiat*, 19, 728-50.
- STORCHI, P. & WOUDSTRA, E. 1995. Calculation models for determining the absorbed dose in water phantoms in off-axis planes of rectangular fields of open and wedged photon beams. *Phys Med Biol*, 40, 511-27.
- STORCHI, P. & WOUDSTRA, E. 1996. Calculation of the absorbed dose distribution due to irregularly shaped photon beams using pencil beam kernels derived from basic beam data. *Phys Med Biol*, 41, 637-56.
- STORCHI, P. R., VAN BATTUM, L. J. & WOUDSTRA, E. 1999. Calculation of a pencil beam kernel from measured photon beam data. *Phys Med Biol*, 44, 2917-28.
- WINICK, H. & DONIACH, S. 1980. *Synchrotron Radiation Research*, New York, Springer US.